

# DYNAMO II: Coupled Stellar and Ionized Gas Kinematics in Two Low Redshift Clumpy Disks

Robert Bassett<sup>1</sup>, Karl Glazebrook<sup>1,2</sup>, David B. Fisher<sup>1</sup>, Andrew W. Green<sup>3</sup>, Emily Wisnioski<sup>4</sup>, Danail Obreschkow<sup>2,5</sup>, Erin Mentuch Cooper<sup>6</sup>, Roberto G. Abraham<sup>7</sup>, Ivana Damjanov<sup>8</sup>, Peter J. McGregor<sup>9</sup>

<sup>1</sup>Centre for Astrophysics and Supercomputing, Swinburne University of Technology, P.O. Box 218, Hawthorn, VIC 3122, Australia

<sup>2</sup>ARC Centre of Excellence for All-sky Astrophysics (CAASTRO)

<sup>3</sup>Australian Astronomical Observatory, P.O. Box 970, North Ryde, NSW 1670, Australia

<sup>4</sup>Max Planck Institute for Extraterrestrial Physics, Garching, Germany

<sup>5</sup>International Centre for Radio Astronomy Research (ICRAR), M468, University of Western Australia, 35 Stirling Hwy, Crawley, WA 6009, Australia

<sup>6</sup>Department of Astronomy, The University of Texas at Austin, Austin, TX 78712, USA

<sup>7</sup>Department of Astronomy & Astrophysics, University of Toronto, 50 St. George St., Toronto, ON M5S 3H8, Canada

<sup>8</sup>Harvard-Smithsonian Center for Astrophysics, 60 Garden St., Cambridge, MA 02138

<sup>9</sup>Research School of Astronomy & Astrophysics, The Australian National University, Cotter Rd., Weston, ACT, Australia, 2611

1 November 2021

## ABSTRACT

We study the spatially resolved stellar kinematics of two star-forming galaxies at  $z \sim 0.1$  from the larger DYNAMO of Newly Assembled Massive Objects (DYNAMO) sample. These galaxies, which have been characterized by high levels of star formation and large ionized gas velocity dispersions, are considered possible analogs to high-redshift clumpy disks. They were observed using the GMOS instrument in integral field spectroscopy (IFS) mode at the Gemini Observatory with high spectral resolution ( $R \simeq 5400$ , equivalent to  $\sigma \simeq 24 \text{ km s}^{-1}$  at the observed wavelengths) and  $\sim 6$  hour exposure times in order to measure the resolved stellar kinematics via absorption lines. We also obtain higher-quality emission line kinematics than previous observations. The spatial resolution (1.2 kpc) is sufficient to show that the ionized gas in these galaxies (as traced by  $H\beta$  emission) is morphologically irregular, forming multiple giant clumps while stellar continuum light is smooth and well described by an exponential profile. Clumpy gas morphologies observed in IFS data are confirmed by complementary narrow band  $H\alpha$  imaging from the Hubble Space Telescope. Morphological differences between the stars and ionized gas are not reflected dynamically as stellar kinematics are found to be closely coupled to the kinematics of the ionized gas: both components are smoothly rotating with large velocity dispersions ( $\sim 40 \text{ km s}^{-1}$ ) suggesting that the high gas dispersions are not primarily driven by star-formation feedback. In addition, the stellar population ages of these galaxies are estimated to be quite young (60–500 Myr). The large velocity dispersions measured for these young stars suggest that we are seeing the formation of thick disks and/or stellar bulges in support of recent models which produce these from clumpy galaxies at high redshift.

**Key words:** galaxies: evolution, stars: kinematics and dynamics.

## 1 INTRODUCTION

Understanding the process of galaxy evolution, particularly in its earliest stages, is a major goal of many research

projects in astrophysics today. Galaxies observed locally are typically near the end of their evolution, having assembled a majority of their stars at high redshift ( $z > 1$ ), closer to

the peak of cosmic star formation (Madau et al. 1996; Lilly et al. 1996; Hopkins & Beacom 2006; Sobral et al. 2012).

Star-forming galaxies at high redshift are often found to be composed of a few large ( $\sim 1$  kpc) star-forming complexes (“clumps”) with high molecular gas content (gas fractions of 20-50%) and high star-formation efficiencies (Daddi et al. 2010; Tacconi et al. 2010; Elmegreen 2011). These complexes are more massive (with typical gas masses of  $10^8 - 10^9 M_\odot$ ) and form stars more efficiently than similar regions observed in the Milky Way (Elmegreen & Elmegreen 2005; Förster Schreiber et al. 2011; Swinbank et al. 2011; Wisnioski et al. 2012). If star forming regions at high redshift obey local scaling relations (Schmidt 1959; Kennicutt 1998), they require high molecular-gas surface densities to fuel the extreme levels of star formation observed (Guo et al. 2012).

Clumpy, irregular galaxies at high redshift have been observed using integral-field spectroscopy (IFS). For studies of galaxy dynamics, IFS data is used to produce detailed two dimensional kinematics maps not possible using traditional spectroscopic techniques. In recent IFS studies, roughly 1/3 of the high-redshift, clumpy galaxies display the random motions expected for galaxies undergoing major mergers. The remainder are either too compact to be reliably classified by the employed methods, or display ordered rotation characteristic of disk galaxies. Disk fractions were found to be 20 – 50% for a number of samples (Genzel et al. 2008; Förster-Schreiber et al. 2009; Law et al. 2009; Wright et al. 2009; Wisnioski et al. 2011). One key observation of clumpy high-redshift disks are large values of velocity dispersion (as high as  $\sim 90 \text{ km s}^{-1}$ ) compared with values of 20-30  $\text{km s}^{-1}$  seen locally (Andersen et al. 2006). Glazebrook (2013) provides a comprehensive review of kinematic studies at high redshift.

The origin and ultimate fate of the clumps in high redshift galaxies is a matter of some debate. In some recent models of galaxy formation, massive high-redshift clumps are shown to spiral inward due to dynamical friction and coalesce into the precursors of local thick disks and galactic bulges (Noguchi 1999; Immeli et al. 2004; Genzel et al. 2008; Dekel et al. 2009; Ceverino, Dekel & Bournaud 2010; Bournaud et al. 2014). Alternatively it has been suggested that star formation feedback in the form of stellar winds and supernovae will cause clumps to be disrupted before migrating to the proto-galactic center (Murray, Quataert & Thompson 2010; Genel et al. 2012). These feedback mechanisms, however, are not well constrained by current observations. In these simulations, the strength and efficiency of the feedback is known to have significant effects on the evolution of simulated high-redshift galaxies (Mandelker et al. 2013). Recent observations of star-forming clumps in high-redshift galaxies have estimated clump lifetimes ranging from 10 to 200 Myr (Elmegreen et al. 2009; Genzel et al. 2011; Newman et al. 2012; Wuyts et al. 2012).

At high redshift, detailed studies of individual clumpy galaxies have been primarily based on observations of ionized gas or broad stellar analysis based on infrared images (Wuyts et al. 2012). Stellar kinematics and ages, which must be measured from absorption features, are too observationally expensive, even using current state of the art facilities. Such observations, however, could be key to distinguishing between models involving clump migration and coalescence

from extreme feedback models in which clumps are rapidly dissolved.

If the large velocity dispersions observed from H $\alpha$  emission are the result of disruptive feedback, we would expect to measure stellar velocity dispersions smaller than those observed for the ionized gas. This would indicate a thick gaseous disk, which has been inflated by strong winds originating from an underlying thinner disk of stars. On the other hand, a key prediction of the turbulent, clumpy disk model is  $\sigma_* = \sigma_{gas}$  which suggests that the stars are formed from an already turbulent medium. Accounting for this initial turbulence may require external sources of gas (e.g., cold accretion or galaxy interactions, Kereš et al. 2005; Bournaud & Elmegreen 2009; Dekel et al. 2009; van de Voort et al. 2011). These external sources of gas may drive turbulence directly or through instabilities commonly associated with gas rich disks (Dekel et al. 2009; Forbes et al. 2013; Bournaud et al. 2014). As of yet, there is no clear consensus on the true fate of giant star-forming clumps, however the above two scenarios are currently the most popular. We note here that in HII regions in the Milky Way, velocity dispersions of the ionized gas and associated young O, B and A stars ( $\sim 5-10 \text{ km s}^{-1}$ ) are found to be lower than those of the stellar thin disk ( $\sim 20 \text{ km s}^{-1}$ ), with the largest values found for the oldest stars (stellar thick disk,  $\sim 40 \text{ km s}^{-1}$ , van der Kruit & Freeman 2011; Pasetto et al. 2012).

While there has been a significant effort to distinguish between clump migration and feedback dominated disk formation models, observing the stellar kinematics at high redshift has not been possible and thus we turn to analogs that we can observe locally. It is important for analogs for this purpose to have high star-formation rates, gas kinematics consistent with turbulent rotating disks, large gas fractions, and clumpy gas morphologies in order to match key features of high-redshift clumpy disks. Studies of low-redshift analogs such as these provide a much greater level of detail and can be used to quantify the effects of resolution and sensitivity on high redshift IFS observations (Gonçalves et al. 2010; Arribas et al. 2014). In previous work (Green et al. 2010, 2014) we have found a sample of low-redshift ( $0.07 < z < 0.14$ ) galaxies with SFRs and kinematics well matched to high-redshift clumpy galaxies. A subsample of these have also been shown from observations with the Plateau de Bure Interferometer to host gas fractions of  $\sim 0.4$  (Fisher et al. submitted).

In this paper we examine stellar and ionized gas morphologies of two  $z \sim 0.1$  disk galaxies which are found to exhibit both ordered rotation and turbulent ionized gas from previous IFS observations (Green et al. 2014). Observations considered here are higher in both signal-to-noise ratio (S/N) and spatial resolution than previous IFS observations of Green et al. (2014) allowing us to perform far more detailed morphological and kinematic analysis. We compare this with previous IFS observations in order to understand the effects of sensitivity and resolution on the results of (Green et al. 2014). Finally, we compare the resolved stellar and ionized gas kinematics of these galaxies in order to understand the sources of turbulence in young galactic disks.

This paper is laid out as follows: In Section 2 we describe our sample and the observations performed for this study, in Section 3 we describe our analysis methodology and present the results, in Section 4 we discuss the impli-

**Table 1.** Physical Properties

ID	$z$	$L(\text{H}\alpha)^1$ (log erg s $^{-1}$ )	$\text{SFR}_{\text{H}\alpha}^2$ ( $\text{M}_{\odot}\text{yr}^{-1}$ )	$\mathcal{M}_{\star}^3$ ( $10^9 \text{M}_{\odot}$ )	$\sigma_{m,\text{SPIRAL}}^4$ (km s $^{-1}$ )	$\mathcal{M}_{\text{gas}}^5$ ( $10^9 \text{M}_{\odot}$ )	b/a $^6$	$i^7$ (degrees)	$h^8$ kpc	$n_b^9$	$h_b^{10}$ kpc
G 4-1	0.129	42.36	41.61	64.74	50.2	43.68	0.85	32.1	2.63	0.4 $\pm$ 0.6	0.2 $\pm$ 0.2
G 20-2	0.141	42.26	17.27	21.56	44.9	19.12	0.88	28.6	2.75	0.5 $\pm$ 0.1	0.52 $\pm$ 0.06

<sup>1</sup>The H $\alpha$  luminosity as measured by previous IFS observations (Green et al. 2014)

<sup>2</sup>The star formation rate measured from previous IFS observations (Green et al. 2014)

<sup>3</sup>The stellar mass reproduced from Kauffmann et al. (2003) scaled by 0.88 to convert from their Kroupa (2001) initial-mass function to that of Chabrier (2003)

<sup>4</sup>Flux weighted gas velocity dispersion from previous IFS observations taken using the SPIRAL IFS

<sup>5</sup>Molecular gas mass inferred from the Kennicutt-Schmidt relation (Green et al. 2014)

<sup>6</sup>axis ratio from 2D surface brightness fitting (GALFIT, Peng et al. 2002) of GMOS continuum maps

<sup>7</sup>Inclination calculated from axis ratios using the standard equation

<sup>8</sup>scale radius measured from exponential fits to combined HST, SDSS, and GMOS data (Section 3.1)

<sup>9</sup>Sérsic index of bulge from fits shown in Figure 3

<sup>10</sup>scale radius of bulge from fits shown in Figure 3

cations of our results, and we provide a brief summary in Section 5. Throughout this work, we adopt a flat cosmology with  $H_0 = 70 \text{ km s}^{-1} \text{ Mpc}^{-1}$  and  $\Omega_M = 0.3$ . This results in a comoving line of sight distance of 533 and 578 Mpc and a spatial scale of 2.29 kpc/'' and 2.46 kpc/'' for galaxies G 4-1 and G 20-2 respectively.

## 2 SAMPLE SELECTION AND OBSERVATIONS

### 2.1 DYNAMO Sample

Recently, Green et al. (2010) identified a sample of low-redshift ( $z \simeq .05 - 0.1$ ) star-forming galaxies, which are possible analogs to high redshift clumpy galaxies. Subsamples of these galaxies have now received extensive multiwavelength observations as part of the DYNAMICS of Newly Assembled Massive Objects (DYNAMO) project. We briefly outline the DYNAMO selection here, however for full sample-selection details see Green et al. (2014).

All DYNAMO galaxies have been classified as star forming in the MPA-JHU Value Added Catalog of the Sloan Digital Sky Survey (SDSS, York et al. 2000). Galaxies hosting active galactic nuclei (AGN) have been excluded based on their position in the Baldwin, Phillips, & Terlevich (BPT, 1981) diagram. The DYNAMO sample includes 67 galaxies with stellar masses ranging from 1.09 to  $65.0 \times 10^9 \text{ M}_{\odot}$  and star-formation rates (SFRs, inferred from H $\alpha$  luminosity of 0.2 to 56.6  $\text{M}_{\odot} \text{ yr}^{-1}$ ) covering typical values found on the main sequence of star formation as well as extremely star-forming galaxies. High H $\alpha$  luminosity galaxies ( $> 10^{41.5} \text{ ergs s}^{-1}$ ) are of particular interest as possible analogs to high-redshift, clumpy galaxies. At low redshift however, they are quite rare (the most likely analogs constitute the upper 95th percentile in H $\alpha$  flux in SDSS DR4).

DYNAMO galaxies were observed using the AAOmega-SPIRAL and Wide Field Spectrograph (WiFeS) IFS ( $0''.7$  and  $1''.0$  spatial sampling respectively with typical seeing of  $1''.0$ - $1''.5$ ). Around one-half of DYNAMO galaxies exhibit regular, rotation-like symmetry. This is comparable to studies at high redshift, such as the SINS survey, in which roughly one-third are classified as rotators, while the remainder are either compact, dispersion-dominated systems or mergers (Förster-Schreiber et al. 2009). Their properties suggest that

highly star-forming, disk-like galaxies in DYNAMO represent a rare, local sample of young, late-type systems, which are in an evolutionary state more common at high redshift ( $z \geq 1$ ).

### 2.2 Absorption Line Subsample

In this paper we focus on two DYNAMO galaxies with smooth rotation and large velocity dispersions, which are similar to star-forming disk galaxies seen at high redshift. Developing accurate dynamical models of these galaxies necessitates the study of their stellar kinematics. This requires observations of stellar absorption lines with spectral resolutions of  $\simeq 20 \text{ km s}^{-1}$  or better, implying significantly longer exposure times than needed for ionized gas kinematics. Studies such as these are currently not possible at high redshift using existing facilities due to the prohibitively long exposure times required.

In addition to long exposure times, we also obtain higher spatial resolution than Green et al. (2014) to allow for studies of effects such as beam smearing. Here we present two galaxies from Green et al. (2014) which were observed using IFS at the Gemini Observatory (programs GS-2012B-Q-88 and GN-2012B-Q-130). These galaxies were selected based on their disk-like kinematics and turbulent ionized gas from previous IFS observations (Green et al. 2014). The physical properties of these galaxies (DYNAMO ID's G 4-1 and G 20-2) are summarized in Table 1.

### 2.3 Observations and Data Reduction

Observations for this study were performed using the Gemini Multi-Object Spectrograph (GMOS, Hook et al. 2004) in the IFS mode (Allington-Smith et al. 2002). In this configuration, the GMOS field of view is comprised of 750 hexagonal fibers, each having a projected diameter of  $0''.2$ . Of these, 500 fibers are used for target observations and are arranged in a rectangular field of view covering  $3''.5 \times 5''.0$ . The remaining 250 fibers are used for dedicated sky observations taken  $1''.0$  from the science position. The detector is made up of three  $2048 \times 4069$  CCD chips separated by  $\sim 0.5 \text{ mm}$  gaps.

Observations presented here were performed at the Gemini South Telescope in October 2011 and January 2012.

The B1200 grating was used which is the highest resolution grating available ( $R \approx 5400$  at the observed wavelengths), giving a dispersion of  $0.24 \text{ \AA}$  per pixel. The average seeing was measured from stars in our acquisition images using the IRAF task *psfmeasure* and was found to be  $0''.5$  (a factor of 3 better than SPIRAL and WiFeS observations). This corresponds to a physical distance of 1.15 and 1.23 kpc at the redshifts of G 4-1 and G 20-2 respectively. This is comparable to the SINS-AO sample which has a typical spatial resolution of 1.6 kpc. Each object was observed at two positions to maximize the spatial coverage. Exposures in each position were dithered spatially as well as spectrally, the latter being achieved by slightly adjusting the grating tilt-angle.

The data was reduced using the Gemini IRAF software package (version 1.9, Turner et al. 2006), which includes bias subtraction, flat-field correction, fiber tracing and extraction, wavelength calibration, and sky subtraction. Motivated by previous studies using similar data (Westmoquette et al. 2007; Liu et al. 2013), we created a custom reduction pipeline that replaces the cosmic ray rejection included in the standard Gemini-GMOS reduction with the Laplacian edge-detection algorithm L.A.Cosmic (van Dokkum 2001). This greatly improves the detection and removal of cosmic rays. This step was performed between bias subtraction and fiber extraction.

The data-reduction process produced an image referred to as a row-stacked spectra (RSS), in which each pixel row corresponds to the spectrum in a single fiber. The RSS images were then resampled by linearly interpolating from the center positions of the hexagonal fibers to create 3D data cubes with  $0''.1$  square pixels. Finally, the individual cubes from each exposure were spectrally resampled onto the same scale. This is necessary due to a slight non-uniformity in  $\Delta\lambda$  between exposures (which is attributed to the spectral dithering). The data cubes were then coadded using a custom IDL script.

We find a number of clear features in our reduced data cubes. The spectral range of the final coadded data cubes varies slightly between our objects, but in the rest-frame of each galaxy the coverage is the same (by design). For each of our objects, the sampled rest-frame wavelengths extend from roughly  $4000 \text{ \AA}$  to  $5350 \text{ \AA}$ . This wavelength range allows us to measure ionized-gas kinematics using three Balmer lines ( $H\beta\lambda 4861 \text{ \AA}$ ,  $H\gamma\lambda 4340 \text{ \AA}$ , and  $H\delta\lambda 4102 \text{ \AA}$ ) and the [OIII] doublet at  $5007 \text{ \AA}$ . Stellar-kinematics measurements are most strongly constrained by absorption associated with the same three Balmer transitions seen in emission but some constraint is also provided by a variety of iron absorption lines throughout this spectral range.

In Section 3.1 we compare morphologies from GMOS IFS to Hubble Space Telescope (HST) FR647M (Proposal ID 12977, PI Damjanov) imaging in which clumps are well resolved. Our HST observations include continuum and  $H\alpha$  imaging. A full description of this data will be included in future work (Fisher et al. in prep). This data illustrates the importance of fully resolving clumps, allowing us to make robust estimates of clump properties such as size and  $H\alpha$  luminosity as well as giving a more reliable measure of clump numbers in our galaxies.

## 3 ANALYSIS AND RESULTS

### 3.1 Mapping Emission: Clumps

We use relative emission-line and continuum strengths to map their baryonic content in order to better understand the structure of our galaxies in comparison with high-redshift clumpy disks. Figure 1 shows false color images of our galaxies. Red corresponds to the median continuum value in each spaxel in the restframe wavelength range of  $\sim 3900\text{-}4200 \text{ \AA}$ , which traces the stellar-mass component. We achieve a continuum signal to noise ratio of  $\sim 15$  and  $\sim 21$  in the central regions of G 4-1 and G 20-2 respectively. The ionized gas is traced in green and blue, indicating the peak value of the  $H\beta$  and [OIII] emission lines, respectively. The scaling of each component was chosen to best illustrate the clumpy substructure of our disk galaxies. The white solid lines correspond to the spatial extent over which we were able to extract information on ionized gas kinematics. Note the irregularity in the central regions of G 20-2 are due to dead fibers in the instrument. Our spatial dithers of  $0''.25$  were not sufficiently large relative to our average seeing ( $\sim 0''.5$ ) to remove this effect. These dead fibers cause problems matching the flux between exposures, but do not affect line-profile shapes and thus will not change our conclusions based on kinematics as these do not depend on accurate fluxes.

In both galaxies we observe a single, centrally located peak in continuum emission, which corresponds spatially with both a peak seen in  $i$ -band imaging from SDSS as well as the galaxies' kinematic centers (see Figures 6 and 8). We indicate these locations with white dashed circles in Figure 1, with diameters equivalent to the seeing of our observations ( $\sim 0''.5$ , equivalent to 1.15 and 1.23 kpc for G 4-1 and G 20-2 respectively). We also observe multiple peaks in emission-line strength, which are offset from the continuum peak. We indicate these in Figure 1 by white arrows. The offsets between the continuum peak and emission line clumps are between 1 and 2 kpc, which is resolved by the seeing of our observations.

Figure 2 shows continuum subtracted  $H\alpha$  maps from HST with  $0''.05$  pixel scale. HST resolution of  $0''.1$  corresponds to a physical distance of 229 pc and 246 pc at the redshifts of G 4-1 and G 20-2 respectively. We identify a number of clumps in the HST  $H\alpha$  maps through visual inspection. These clumps range in luminosity from  $10^{40}$  to  $10^{42} \text{ ergs s}^{-1}$  indicating SFRs of  $\sim 1\text{-}10 M_{\odot} \text{ yr}^{-1}$ . These numbers are consistent with the properties of clumps observed in  $z \sim 2$  disk galaxies (Genzel et al. 2011). A detailed study of the clump properties using the HST photometry will be the subject of future work by the DYNAMO team (Fisher et al. in prep).

Comparing Figures 1 and 2 we find that clumps in the HST imaging are more easily distinguished. Some clumps identified from GMOS-IFS data correspond to single clumps from HST while others are unresolved collections of multiple clumps. Clump sizes are smaller than would be indicated from GMOS-IFS, however, most clumps are well resolved by HST giving a lower limit to their sizes of 250 pc (HST resolution at  $z = 0.13$ ). This shows that the comparison between our low-redshift IFS data and high-resolution, space-based imaging will be valuable for the interpretation of similar studies at high redshift.

In Figure 3, we show the surface-brightness profiles of

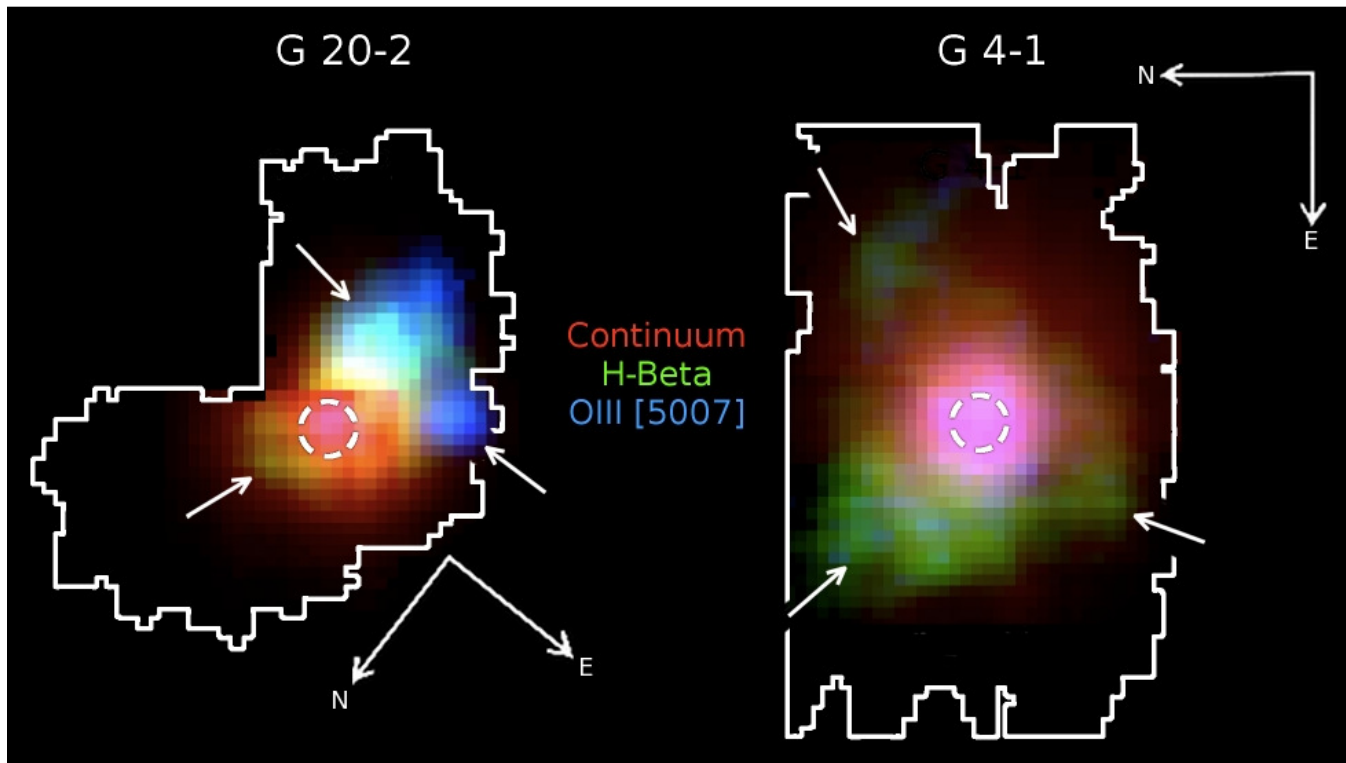


**Figure 1.** False color images of our disk galaxies. Red corresponds to the median continuum level (rest frame B band) while green and blue show the peak flux of the  $H\beta$  and  $[OIII]$  (5007 Å) emission lines respectively. The color scaling is not the same between components, but is chosen to highlight substructure of our disk galaxies. The peak of the continuum emission is marked by a dashed circle with a diameter equivalent to the average seeing of our observations ( $\sim 0''.5 \simeq 1.1$  kpc at  $z = 0.14$ ). In both galaxies the continuum peak location is coincident with the kinematic center (see Figure 6). Both galaxies exhibit multiple large clumps of gas which are offset from the central continuum clump by a distance which is approximately equal to the seeing of our observations. The locations of the clumps are marked with white arrows. We note the irregularities in the central regions of G 20-2 which are due to dead fibers in the detector obscuring the central region in multiple exposures. Overplotted are the footprints of Figure 6 in white which indicate the area over which we can reliably extract ionized gas kinematics from our datacubes.

the star light for both target galaxies. These profiles are composite surface-brightness profiles of HST FR647M, SDSS  $i$  and continuum emission from our GMOS observations (see Figure 1). The surface photometry from each telescope is scaled and combined using the method of Fisher & Drory (2008). This method reduces random errors (e.g., sky subtraction) and allows us to probe surface-brightness profiles to larger radius. The stellar emission is smooth, and the main body of both galaxies ( $r \geq 1.5$  kpc) are well described by exponential surface-brightness profiles at large radii, suggesting that these are unperturbed disks (van der Kruit & Freeman 2011). We determine scale lengths of 2.75 and 2.63 kpc for G 20-2 and G 4-1 respectively, these values are also included in Table 1. Both galaxies have bulges in their continuum emission. We indicate our bulge-disk decomposition with red lines. The bulges in these galaxies appear to be co-located with rises in the velocity-dispersion maps of Figure 6. The central kinematic component will be discussed in more detail in Section 3.4.

In Figure 4, we make a qualitative comparison between the spectra in different regions. We show two spectra, each in artificial apertures with diameter equal to  $0''.5$ . The first is centered on the continuum peak and the second is located at the peak of  $H\beta$  flux from our GMOS datacubes. Figure 4 shows a small section of these spectra centered between

$H\delta$  and  $H\gamma$  for galaxy G 20-2 (spectra for G 4-1 are qualitatively very similar). These spectra have been normalized by the median continuum value for direct comparison. Although not apparent in Figure 1, Figure 4 clearly shows that we observe significant line emission even in the central regions. The one difference between the two regions is a much higher emission-line equivalent width in the emission-line region, apparent in the difference plot (bottom panel of Figure 4). This is not surprising as the regions in which the emission lines are strongest are not coincident with the peak in continuum flux.

The emission-line-region spectrum has a lower S/N ratio due to the lower continuum surface brightness, but the overall continuum shape is nearly identical to that of the peak continuum region. This suggests that the regions in which we can reliably observe absorption-line profiles host similar aged stellar populations. This could partially be an effect of the seeing in which age differences are smeared out. We also note that it is quite difficult to probe stellar populations in the regions of maximum  $H\beta$  equivalent width (where the average stellar age is likely to be the lowest) due to the exponentially-dropping continuum surface brightness.

By examining the ionized gas and continuum components of G 4-1 and G 20-2 we provide further evidence that these galaxies are excellent low-redshift analogs to

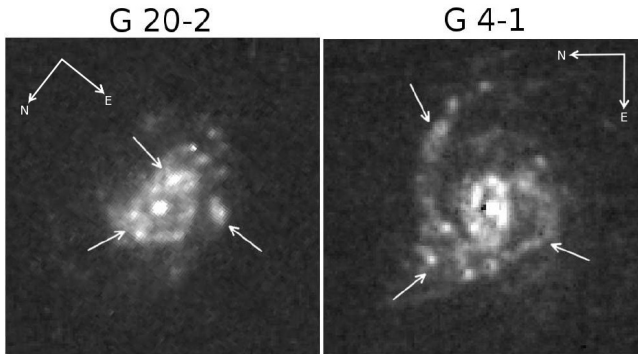


**Figure 2.** Continuum subtracted  $H\alpha$  maps from HST with  $0''.05$  pixel scale. HST resolution of  $0''.1$  corresponds to a physical distance of 229 pc and 246 pc at the redshift of G 4-1 and G 20-2 respectively. Comparing with Figure 1 we find that clumps in the HST imaging are more easily distinguished. While some clumps identified from GMOS-IFS data are matched to single clumps here, others are found to be unresolved collections of multiple clumps. While clump sizes are smaller than would be predicted from GMOS-IFS, most clumps are resolved by HST providing a lower limit to their sizes of 250 pc. The white arrows indicate the same clump locations shown in Figure 1. Comparisons between our low redshift IFS data and high-resolution, space-based imaging will be valuable for the interpretation of similar studies at high redshift.

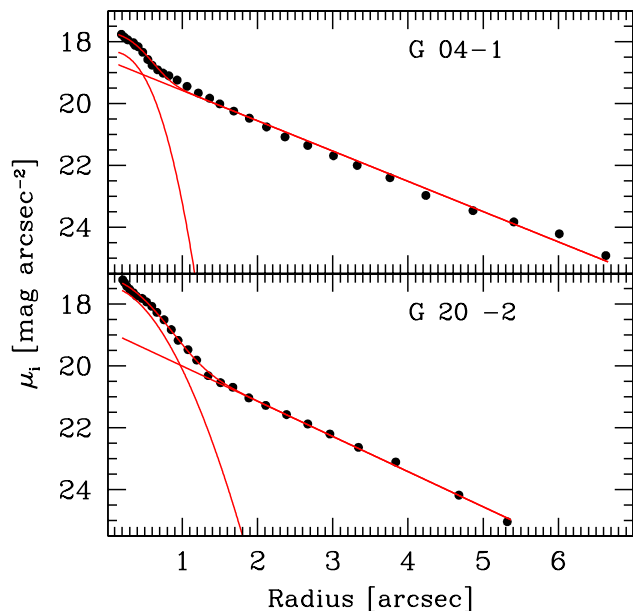


**Figure 3.** Surface brightness profiles of continuum emission for the two target galaxies, G 04-2 (top) and G 20-2 (bottom). The flux of the continuum maps of both profiles has been scaled to match that of SDSS  $i$  band profile. The solid dots represent isophotes and the red line represent a Sérsic function bulge plus exponential disk fit to the surface brightness profile. For each galaxy there is a “bulge” in the surface brightness profile that is co-located with the rise in velocity dispersion in our kinematic maps (Figure 6). Some galaxy properties from these fits are included in Table 1.

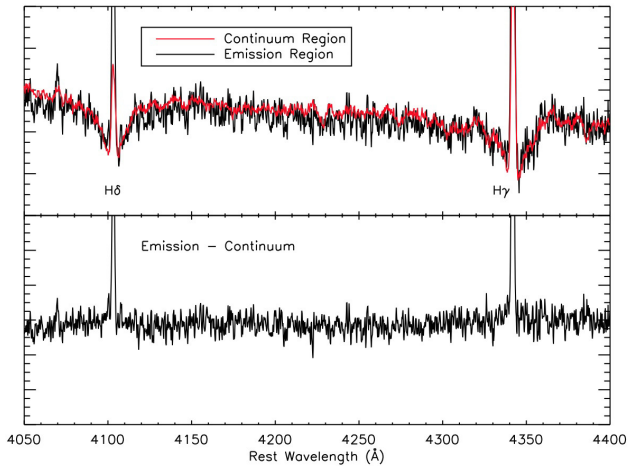


**Figure 4.** Comparison between spectra observed in the continuum peak and the brightest  $H\beta$  clump of G 20-2, identified from our GMOS datacubes, summed in a  $0''.5$  aperture centered on these regions and normalized by the median continuum level. Our spectra are characterized by strong emission lines, in particular [OIII] and Balmer lines, as well as strong Balmer absorption associated with A-type stars. The top panel shows the continuum peak spectrum in red over the emission line peak spectrum in black, while the bottom shows the continuum peak spectrum subtracted from that of the emission line peak. Here we show a section of our observed spectral range which includes the  $H\gamma$  and  $H\delta$  absorption lines, which (along with  $H\beta$ ) are the strongest we observe. The shape of the Balmer absorption lines in both are quite similar, suggesting that the underlying stellar populations in both regions are of comparable age. The major difference between the spectra is the equivalent width of the emission lines as seen in the bottom panel. This is not surprising as the regions in which the emission lines are strongest are not coincident with the peak in continuum flux.

high-redshift clumpy disks. We find that the ionized gas is arranged in multiple clumps surrounding a central continuum peak. We show that clumps are marginally resolved, but that our  $0''.1$  HST imaging will be required to measure accurate sizes for these clumps. Surface brightness profile fitting to combined HST, GMOS, and SDSS data shows that both galaxies are well described by an exponential at large radii with evidence of a small bulge.

### 3.2 Matching Templates with Observed Spectra

We employed the full spectrum stellar-kinematics fitting program Penalized Pixel-Fitting (pPXF, Cappellari & Emsellem 2004) to measure the velocity and velocity dispersion of the stellar populations in our sample. We fit our observations using synthetic galaxy spectra created with the PÉGAISE-HR code (Le Borgne et al. 2004). This code uses high-resolution ( $R=10,000$ ) stellar spectra from the ÉLODIE library (Prugniel & Soubiran 2001) to construct an evolutionary sequence of composite spectra based on simple stellar populations (SSPs) with ages ranging from 10 Myr to 20 Gyr.

We first developed a test to select the PÉGAISE template with an SSP age most similar to our observed spec-

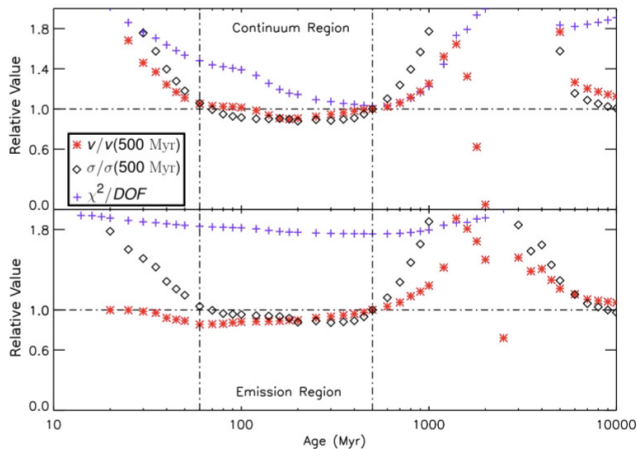


**Figure 5.** Velocity and velocity dispersion measurements of stellar kinematics for spectra shown in Figure 4 at each template age (as described in Section 3.2). Both kinematics measures are normalized by measurements made using templates with ages of 500 Myr. We have overplotted a dot-dashed line on the vertical axis at 1 for reference. We find in the age range from 60 to 500 Myr (indicated by vertical dot-dashed lines) measurements of stellar kinematics remain relatively stable. We have also overplotted the  $\chi^2/\text{DOF}$  (not normalized) for each template and find that this range also corresponds to the statistically best fitting templates. We adopt a template age of 500 Myr for fitting stellar kinematics in this study as this corresponds to the  $\chi^2/\text{DOF}$  closest to 1 for both regions.

tra. Selecting a spectral template that is well matched to the observed spectra is essential in reliably extracting kinematics through full spectrum fitting. This is because of the wide range of absorption line profiles associated with different stellar populations. Our test involves using pPXF to fit the representative spectra considered in Section 3.1 (see Figure 4) with each PÉGASE-HR template individually while masking the emission lines. This procedure measures the velocity, velocity dispersion, and goodness of fit ( $\chi^2/\text{DOF}$ ) at each SSP template age. We performed this test on spectra from both the continuum and emission line peaks to check for any spatial variation in stellar population age. We then selected the template with  $\chi^2/\text{DOF}$  closest to 1. The results of template selection are shown in Figure 5. Kinematic values presented have been normalized by the measurement made using a template age of 500 Myr.

Figure 5 shows that there is a range in template ages between 60 and 500 Myrs in which both the stellar velocity and velocity dispersion measurements remain relatively stable. The  $\chi^2/\text{DOF}$  values indicate that templates in this age range are the best fitting from the PÉGASE-HR library (this is also apparent from visual inspection of individual fits). This is true for both the continuum and emission line peaks suggesting that there is no evidence of spatial variations in stellar population ages in our observations.

We investigated the effects of repeating our stellar kinematics fitting (results presented in Figure 8) using each templates in the age range from 60-500 Myr individually. Selecting templates in the age range of 100-500 Myr returns velocity and velocity dispersion measurements in agreement with measurements using a 500 Myr old template within our simulated uncertainties (discussed in Section 3.3.4). At

younger template ages, the velocity remains in agreement while the velocity dispersion measurement increases relative to measurements made using 500 Myr old templates. This difference increases as template age decreases from a  $\sim 5\%$  increase in velocity dispersion using a 100 Myr template to a  $\sim 38\%$  increase from fits performed with a 60 Myr template.

Qualitatively it is reasonable to expect the continuum emission from these galaxies in this wavelength regime to be dominated by young stellar populations because the extreme levels of line emission are indicative of a recent (and likely ongoing) star formation activity. A PÉGASE-HR template with an age of 500 Myr is selected for stellar kinematics measurements throughout the remainder of this paper. This was chosen as fits using templates aged 500 Myr display the nearest  $\chi^2/\text{DOF}$  value to 1 in both the continuum and emission line regions for both galaxies.

### 3.3 Measuring Kinematics

#### 3.3.1 High Resolution Ionized-Gas Kinematics

We produced ionized gas velocity and velocity dispersion maps by fitting a single Gaussian profile to the  $\text{H}\beta$  emission line. The velocity and velocity dispersion are then calculated using the centroid position and  $\sigma_{gas}$  of the model fit. To correct for instrumental broadening, we subtracted the instrumental line width from the raw measurement in quadrature:  $\sigma_{gas} = \sqrt{\sigma_{obs}^2 - \sigma_{inst}^2}$ , where  $\sigma_{obs}$  is the observed velocity dispersion and  $\sigma_{inst}$  is the instrumental broadening measured from our arc observations to be  $24 \text{ km s}^{-1}$ . Figure 6 shows the results of this procedure.

We employ the Voronoi Binning method of Cappellari & Copin (2003) in order to extend this analysis to radii beyond which these measurements from single spaxels are reliable. This technique uses maps of S/N to ensure that each spatial bin falls above a specified S/N threshold. For our inputs we use the continuum maps of our galaxies from Figure 1 and a constant noise based on the variance of our spectra in off target regions. Because the line emission is significantly stronger than that of the continuum we use a low S/N threshold of 1.0, however many bins (particularly those at the center) have S/N much higher than this. We choose to use continuum S/N rather than emission-line S/N because the clumpy structure results in oddly shaped bins which distort the kinematic maps. Our low S/N threshold ensures that within the region in which we observe clumps, all Voronoi bins contain a single spaxel.

We used our kinematics maps to measure global  $\sigma$  values which we compare with previous results. The ionized-gas-velocity maps we produced from our GMOS observations extend into the flat portion of the rotation curve (which is shown later in Section 3.6) where beam-smearing effects are minimized. This allows for robust measurements of velocity dispersion. We took an average value of the outer bins to make an estimate of the velocity-dispersion value across the disk. We indicate the bins over which these averages were taken by black lines in the bottom panel of Figure 6. These bins correspond to regions that are a distance equivalent to our seeing away from the kinematic centers of our galaxies. This results in mean  $\text{H}\beta$  dispersions of  $36.6 \text{ km s}^{-1}$  and  $29.8 \text{ km s}^{-1}$  for G 20-2 and G 4-1, respectively. We consider these our best estimates of the overall disk veloc-

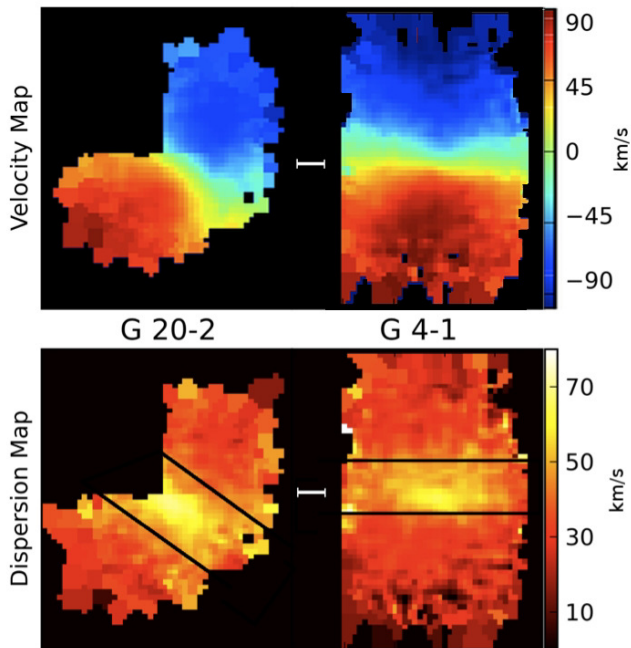


**Figure 6.** Velocity and velocity dispersion maps for the ionized gas component of our sample measured by fitting a Gaussian profile to the  $H\beta$  emission line. The small white bars represent a distance of  $\sim 1.5$  kpc at each galaxy’s redshift. Both galaxies display smoothly varying velocity fields and centrally peaked velocity dispersions typical of disk galaxies. The velocity dispersions here are large relative to typical disk galaxies nearby ( $5\text{--}20$   $\text{km s}^{-1}$  from DISKMASS, Andersen et al. 2006) suggesting that the gas disks in these galaxies are highly turbulent. The black lines shown in the bottom row mark the boundaries of the “central region” which exhibits increased velocity dispersion. These regions possibly represent a young galactic bulge while velocity dispersions in the outer bins are characteristic of a marginally stable, turbulent disk. We measure a mean ionized gas velocity dispersion of  $36.6$   $\text{km s}^{-1}$  and  $29.8$   $\text{km s}^{-1}$  for the outer regions of G 20-2 and G 4-1 respectively. See Section 3.4 for further discussion of global  $\sigma$  estimates.

ity dispersion and compare them with velocity dispersions of local disks in Section 4.1.

We also took a raw averages without excluding central bins to compare with previous work (Green et al. 2014). This results in values of  $43.2$   $\text{km s}^{-1}$  and  $35.6$   $\text{km s}^{-1}$ . For G 20-2 this is much closer to the value of  $44.9$   $\text{km s}^{-1}$  found from SPIRAL data, while the dispersion measured for G 4-1 is significantly lower ( $\sigma_{\text{SPIRAL},m} = 50.2$   $\text{km s}^{-1}$ ).

We performed a test to see if the difference between our GMOS and SPIRAL results is an effect of spatial resolution. We resample our GMOS datacubes to the resolution of the previous SPIRAL observations and follow the same Gaussian fitting procedure outlined above. We then calculated a flux weighted velocity dispersion (matching the analysis of Green et al. 2014) for both galaxies resulting in  $\sigma_m$  of  $45.3$  and  $38.8$   $\text{km s}^{-1}$  for G 20-2 and G 4-1. For G 20-2,  $\sigma_m$  is well matched to the value calculated from SPIRAL data, while our measurement for G 4-1 is still  $10$   $\text{km s}^{-1}$  less than previous measurements.

The remaining difference of  $10$   $\text{km s}^{-1}$  between GMOS and SPIRAL measurements for G 4-1 (as well as the  $10\text{--}20$   $\text{km s}^{-1}$  difference between  $\sigma_m$  of Green et al. (2014) and

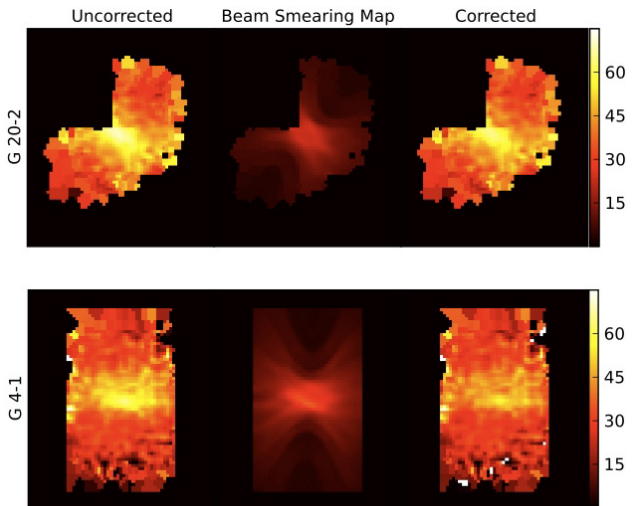


**Figure 7.** Modeling the effects of beam smearing. Plots for each disk galaxy are shown in a single row. From left to right each row shows maps of velocity dispersion corrected for instrumental broadening, a simulated map of the influence of beam smearing (described in Section 3.3.2), and velocity dispersion maps corrected for beam smearing by subtracting the central panel from the left panel in quadrature. It is seen that the influence of beam smearing peaks at the centers of our galaxies as expected. Beam smearing estimates in these regions are  $24\text{--}36$   $\text{km s}^{-1}$  and the peak measured velocity dispersions are  $\sim 70$   $\text{km s}^{-1}$ . The applied correction here is around  $4\text{--}8$   $\text{km s}^{-1}$  showing that even at the centers of our galaxies this is a minimal effect. In the outer portions of our disks the influence of beam smearing can effectively be ignored.

our mean  $\sigma_{gas}$  excluding central bins) can be attributed to a bias of the previous SPIRAL measurements towards regions of highest  $H\alpha$  flux due to the lower sensitivity of previous observations. This means that our  $\sigma_m$  values from SPIRAL observations contain little or no contribution from dynamically cooler gas at large radii. Additionally, if the most intense line emission is coincident with the kinematic center of a galaxy, then our previous measurements will be more strongly influenced by beam smearing as the central region is where velocity gradients will be at a maximum. This is the case for galaxy G 4-1 while in G 20-2 the most intense line emission is offset from the kinematic center (see Figures 1 and 6).

In summary, discrepancies between  $\sigma_m$  measurements from SPIRAL and GMOS can largely be attributed to spatial resolution, sensitivity, and beam smearing. We note that our GMOS dispersions are consistent with higher resolution kinematics maps based on Paschen  $\alpha$  from adaptive optics assisted observations using the OH-Suppressing Infrared IFS (OSIRIS) on Keck (Bassett et al. in prep). A more detailed analysis of global velocity dispersions can be found in Section 3.4.

### 3.3.2 Modeling the Effects of Beam Smearing

While the GMOS observations presented here benefit from improved spatial resolution, beam smearing can still play an important role in understanding our kinematic measurements. Davies et al. (2011) shows how typical observations



of  $z \sim 0.1$  galaxies at  $\sim 1''$  resolution can inflate the velocity dispersion of average disk galaxies ( $\sim 10 - 25 \text{ km s}^{-1}$ , Andersen et al. 2006; Martinsson et al. 2013) to the large values found here.

Beam smearing affects both the observed velocity and velocity-dispersion maps due to velocity gradients over individual beams. The end result is a slight reduction in the slope of rotation curves and an inflation of velocity-dispersion measurements. This effect is most pronounced in the central regions of disk galaxies, where velocity gradients are at a maximum. We can attempt to correct for this by carefully considering the observed shape of the velocity field as well as the average seeing of our observations.

We performed a simulation to better understand quantitatively the effects of beam smearing on our velocity-dispersion measurements. We first fit a rotating disk model to the observed ionized gas kinematics, the details of which can be found in Green et al. (2014). We mapped the influence of beam smearing on these models when subject to conditions typical of our observations ( $\sim 0''.5$  seeing). This mapping was done by creating an artificial datacube with two spatial dimensions and one velocity, with the velocity resolution chosen to match our observations. The velocity distribution of each artificial spaxel received a contribution from every other spaxel weighted by a two dimensional Gaussian function with  $\sigma$  equal to our average seeing. The velocity distribution was subsequently fit with a Gaussian function and the  $\sigma$  of these fits were taken as the contribution of beam smearing to our measured velocity dispersions.

We subtracted the produced “beam smearing maps” in quadrature from the observed velocity-dispersion maps to correct for the beam-smearing effect in our velocity dispersion maps (Gnerucci et al. 2011; Epinat et al. 2012). Maps of our modeled beam smearing and the corrected velocity dispersion are shown in Figure 7. From the central figure in each row it is seen that the estimated influence of beam smearing peaks as expected in the central region, where the velocity gradient is at a maximum. Typical values in the central regions of our beam-smearing maps are  $24\text{-}30 \text{ km s}^{-1}$ , which is low relative to measured velocity dispersions in the same regions ( $55\text{-}80 \text{ km s}^{-1}$ ).

We also compared the central beam-smearing estimates with a simple analytic calculation. We assumed a linear velocity gradient and constant intensity, which is a reasonable approximation for the central regions of smoothly rotating disks. We estimated a central velocity gradient from Figure 6 of  $5\text{-}6 \text{ km s}^{-1} \text{ pixel}^{-1}$  by measuring the difference in velocity between the two flat portions of the rotation curves and dividing by the separation between these two portions in pixels. The contribution of beam smearing was then estimated as

$$\sigma_{BS} \approx \frac{dV}{d\theta} \sigma_{\theta}, \quad (1)$$

where  $d\theta$  is a distance corresponding to one pixel and  $\sigma_{\theta}$  is the seeing of our observations in pixels ( $\sim 5$  pixels). This results in a value of  $25\text{-}30 \text{ km s}^{-1}$ , consistent with the modeled values.

When the modeled beam-smearing contribution is subtracted in quadrature from the observed velocity dispersion in the regions of maximum velocity dispersion ( $55\text{-}80 \text{ km}$

$\text{s}^{-1}$ ), the correction is only  $4\text{-}8 \text{ km s}^{-1}$ , comparable to our errors in stellar-kinematics measurements (see Section 3.3.4). This small correction suggests that the increased velocity dispersion in the central regions are real and a possible signature of a small bulge or pseudobulge (see Section 4.4 for discussion). Furthermore, in regions further than our seeing distance from the central regions, beam smearing can effectively be ignored.

### 3.3.3 Mapping Stellar Kinematics

In this section, we map the stellar kinematics of our galaxies and compare them directly to those of the ionized gas. We again employed the Voronoi Binning method of Cappellari & Copin (2003) to ensure that our measurements are reliable even in the faint outskirts of our galaxies. We used the same setup as in Section 3.3.1, but with a larger S/N threshold of 10. We used a larger S/N threshold here because the absorption signal is much weaker than the emission line strength.

We developed a custom IDL wrapper for pPXF which simultaneously fits for stellar and emission-line kinematics. This allows us to directly compare stellar and gas kinematics on a bin-by-bin basis. We first fitted the spectrum with pPXF using emission-line masking and subtracted the resulting fit. The result is a spectrum composed only of emission lines. Next, we fit the emission lines using a single Gaussian profile. From the centroid position and  $\sigma$  of these fits we again measured the velocity and velocity dispersion of the ionized gas in our galaxies.

We plot the results of our stellar-kinematics fitting procedure in Figure 8. For each galaxy, the velocity maps of the ionized gas and stars, as well as the subtracted residual of  $v_{gas} - v_*$ , are shown in the top row. Similarly, the bottom row shows the maps of velocity dispersion, but this time showing the absolute difference:  $|\sigma_{gas} - \sigma_*|$ . This allows us to plot using the same color bar used for the velocity-dispersion maps, however we note that in most bins the stellar velocity dispersions is larger than that of the gas (see Figure 10). Also depicted in the top row of Figure 8 as solid white lines are the footprints of the gas only kinematics measurements from Figure 6 for comparison. These footprints indicate the extent to which we can reliably measure ionized gas kinematics. Solid black lines in the bottom row differentiate bins that are considered part of the central region and those that are part of the outer disk. Global  $\sigma$  values are calculated for these regions and discussed in Section 3.4.

### 3.3.4 Stellar Kinematics Uncertainties

We next consider if the residual-kinematic maps (right columns for both galaxies in Figure 8) are significant or if they are within our measurement uncertainties. Following the procedure suggested by Cappellari & Emsellem (2004), we performed a Monte Carlo simulation of our absorption fitting routine. This simulation was done by first subtracting the best-fit spectrum output by pPXF, from the original spectrum, to produce a residual spectrum. The residual spectrum was then randomized in wavelength (using the IDL task SHUFFLE), and added to the best fit in order to simulate an idealized spectrum with noise characteristic of our

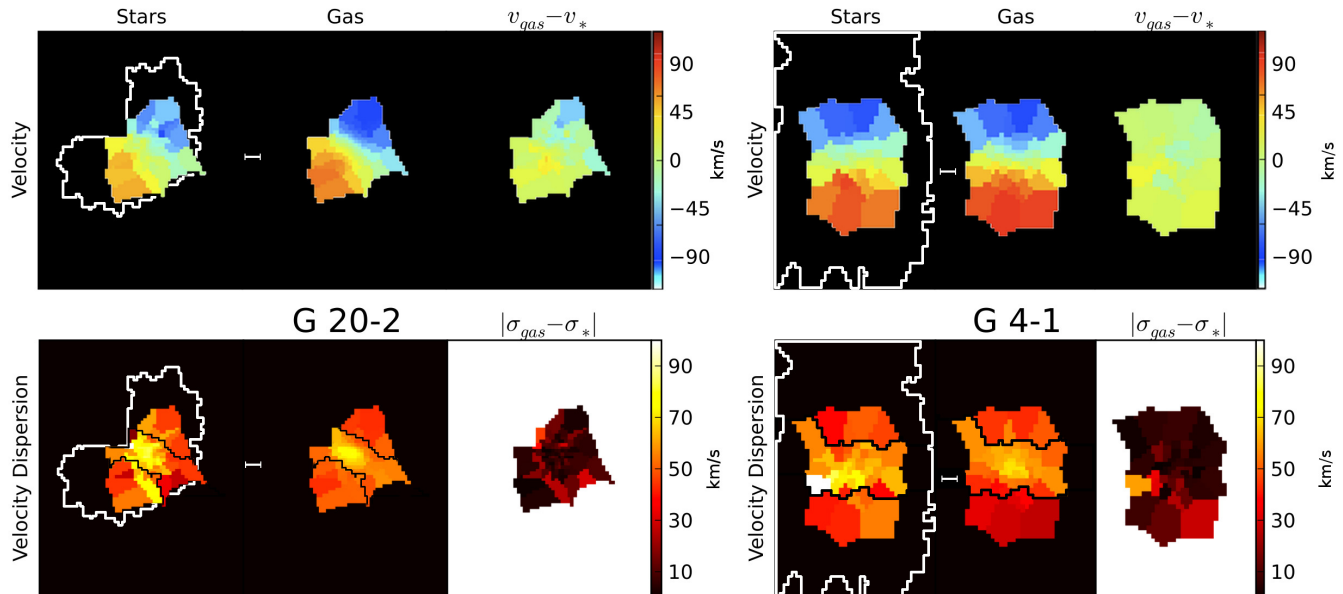


**Figure 8.** Results of pPXF measurements of stellar kinematics in our sample. In order to obtain reliable measurements in the faint outskirts of these galaxies, the Voronoi Tessellated binning method was employed. The gas velocity was remeasured in each bin for direct comparison. White bars in each panel correspond to a distance of  $\sim 1.5$  kpc at the redshift of our galaxies. The velocity maps are plotted over the footprint of the gas only measurements for comparison. The gas and stars in these galaxies appear to be closely kinematically coupled, both are arranged in a smoothly rotating disk with a large velocity dispersion. We calculate a mean stellar velocity dispersion value for both the gas and stars, excluding central regions (indicated by black lines in the velocity dispersion maps) for use in simple disk models. This results in values of  $\sigma_{d,*} = 52.8$  for G 20-2 and  $\sigma_{d,*} = 47.5$  for G 4-1. See Section 3.4 for further discussion of global sigma values

**Table 2.** Stellar Kinematics Uncertainties

	Velocity Uncertainty $\pm \text{km s}^{-1}$	$\sigma$ Uncertainty $\pm \text{km s}^{-1}$
G 4-1 center	4.7	5.2
G4-1 disk	6.7	7.9
G 20-2 center	5.0	5.9
G 20-2 disk	6.7	8.2

observations. We chose to add the shuffled residual to the model rather than the original spectrum as the latter tends to produce spectra which are noisier than the original, thus overestimating the uncertainty. Some areas of the spectra display unusually large residuals due to the chip gaps in the detector (which are masked out in the fitting procedure). To account for these large deviations we replace values in masked regions by random values based on the standard deviation of the unmasked regions of the residual spectrum.

We produced 1000 simulated spectra for each spatial bin and refit each of them using the same pPXF setup. We then computed the standard deviations of the sample of simulated fit values (using the square root of the IDL VARIANCE task). These values were taken as our uncertainties in each bin. Figure 9 shows the maps of our uncertainties in velocity and velocity dispersion for G 20-2 and G 4-1. Our measurements are most accurate in the centers of our galaxies, where the continuum strength is the highest. The centers

are also the areas in which the effects of beam smearing are the greatest.

Due to the sensitivity and high spectral resolution of our observations, even measurements of the stellar kinematics made at the largest radii are quite robust. We estimate the measurement uncertainty of our pPXF procedure by taking two mean values for both stellar velocity and velocity dispersion. One measurement in the central regions and one in the outer bins. Central and outer regions are defined as in Section 3.3.3 and Figure 8. These values are presented in Table 2. Kinematics measurements in most bins are known within  $\pm 8 \text{ km s}^{-1}$  based on our Monte Carlo simulation.

Comparing Figures 8 and 9 one can see that kinematics for these two components match quite closely. The mean values of  $|v_{gas} - v_*|$  and  $|\sigma_{gas} - \sigma_*|$  are 15.8 and 8.4  $\text{km s}^{-1}$  for G 20-2 and 8.9 and 8.3  $\text{km s}^{-1}$  for G 4-1 mostly consistent with our estimated stellar kinematics uncertainties. The large velocity difference in G 20-2 between stars and gas may be attributed to asymmetric drift. This is a phenomenon observed in many late-type galaxies in which the stellar disk lags behind the gas disk due to extra support from random motions (Golubov et al. 2013, some evidence for this can be seen in Figure 10).

We find that the ionized gas and stellar kinematics of these galaxies are closely coupled and characterized by smooth rotation and large, centrally peaked velocity dispersions. It is interesting that these two components are so well matched kinematically while their morphologies (shown in Figure 1) appear very different.

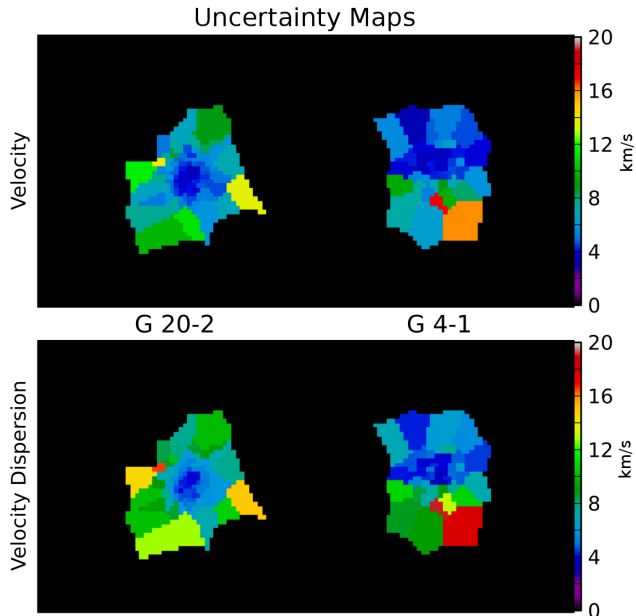


**Figure 9.** To estimate the uncertainties of our pPXF measurements, we perform a Monte Carlo simulation as suggested by Cappellari & Emsellem (2004). Briefly the residual of our stellar kinematics fits are shuffled and added to the best fit model. We then refit this spectrum with the original model in an attempt to recover the known input kinematics. This process is repeated 1000 times for each spatial bin and the uncertainties are taken as the standard deviation of these measurements. Due to the high resolution of our spectra and the sensitivity of our observations, we are able to make measurements of stellar kinematics accurate to  $5 - 8 \text{ km s}^{-1}$  in most bins.

**Table 3.** Global Beam-Smearing Corrected  $\sigma$  Values

Galaxy	$\sigma_{m,\text{SPIRAL}}^1$ $\text{km s}^{-1}$	$\sigma_{c,\text{gas}}^2$ $\text{km s}^{-1}$	$\sigma_{c,*}^3$ $\text{km s}^{-1}$	$\sigma_{d,\text{gas}}^4$ $\text{km s}^{-1}$	$\sigma_{d,*}^5$ $\text{km s}^{-1}$
G 4-1	50	44	$58 \pm 5$	30	$48 \pm 8$
G 20-2	45	49	$66 \pm 6$	37	$53 \pm 8$

<sup>1</sup>Flux-weighted mean ionized-gas velocity dispersion measured from H $\alpha$  emission lines (Green et al. 2014)

<sup>2</sup>Unweighted-mean ionized-gas velocity dispersion of central regions measured from H $\beta$  emission observed with GMOS-IFS

<sup>3</sup>Unweighted-mean stellar velocity dispersion of central regions from pPXF fits to GMOS-IFS data

<sup>4</sup>Unweighted-mean ionized-gas velocity dispersion of disk regions measured from H $\beta$  emission observed with GMOS-IFS

<sup>5</sup>Unweighted-mean stellar velocity dispersion of disk regions from pPXF fits to GMOS-IFS data

### 3.4 Global Velocity Dispersion Estimates

We find that our disk galaxies exhibit enhanced velocity dispersions in their central regions, which can not entirely be attributed to the effects of beam smearing. Regions of enhanced velocity dispersion correspond to a central excess in stellar light compared with a single exponential profile (see Figure 3). This is possible evidence for a galactic bulge and thus we calculated two average velocity dispersions for both the stellar and ionized gas components: one mean in the cen-

tral regions ( $\sigma_c$ ) and one in the outer regions ( $\sigma_d$ ). These two values correspond to a “bulge” and “disk” mean  $\sigma$  respectively. Different regions for calculating mean  $\sigma$  values are indicated in the velocity dispersion maps of Figures 6 and 8 by solid black lines. We also calculated the average influence of beam smearing in the central and outer regions. This was done by taking an average of pixels from our beam-smearing maps (Figure 7) in each of the Voronoi Bins of Figures 6 and 8. We then average these binned-beam-smearing values in the same way as was done for the velocity-dispersion measurements. A correction is then applied to the respective mean velocity-dispersion values as  $(\sigma_{mean}^2 - \sigma_{BS}^2)^{\frac{1}{2}}$ .

We first consider the mean velocity-dispersion values of the central bins,  $\sigma_c$ . The resulting values are shown in Table 3. The measurements made are the mean ionized-gas velocity dispersion from gas-only measurements ( $\sigma_{c,\text{gas}}$ ) and the mean stellar velocity dispersion ( $\sigma_{c,*}$ ). We also include for comparison  $\sigma_{m,\text{SPIRAL}}$  which is the flux weighted mean ionized gas velocity dispersion from Green et al. (2014). In both galaxies, the values of  $\sigma_{c,*}$  are larger than  $\sigma_{c,\text{gas}}$ . The differences are  $17.7$  and  $14.5 \text{ km s}^{-1}$  for G 20-2 and G 4-1, respectively. This can be attributed to the fact that in our simple mean each Voronoi bin is given the same weight. Because our data cubes are more coarsely binned during our pPXF procedure, the outer regions (where velocity dispersion are lowest) are given less weight per unit area in  $\sigma_{c,*}$  than in  $\sigma_{c,\text{gas}}$ . When Voronoi bins are also weighted by bin size, this difference is reduced by half.

We next make similar measurements considering the outer disk regions of  $\sigma_{d,\text{gas}}$  and  $\sigma_{d,*}$ . These results are shown in Table 3. Similar to the central regions, our measurements of  $\sigma_{d,*}$  are larger than  $\sigma_{d,\text{gas}}$  by  $16.2$  and  $17.7 \text{ km s}^{-1}$  for G 20-2 and G 4-1, respectively. The difference in this case is likely due to the reduced spatial coverage of our pPXF kinematics (see Figure 8) which are restricted to the largest  $\sigma$  regions of the galactic disks.

### 3.5 Rotation Curves

The main result of this study is that in both galaxies, *the stellar kinematics closely mirror those of the ionized gas*. This is shown again in Figure 10 where we plot our kinematics measurements versus distance to the galactic center. In the top panels we have computed  $V(r)$  in each spatial bin using  $V(r, \phi) = V(r) \cos(\theta) \sin(i)$  (Warner, Wright & Baldwin 1973) where  $\theta$  is the azimuthal angle in the galactic plane measured from the kinematic major axis and  $i$  is the inclination. In the bottom panels we plot velocity dispersions after correcting for beam smearing by subtracting our simulated beam smearing contribution (see Section 3.3.2) from the measured velocity dispersion in quadrature on a bin-by-bin basis.

We estimated the inclinations of our galaxies,  $i$ , from axis ratios determined using GALFIT (Peng et al. 2002). We performed this fit on continuum images created from our data cubes but taking the median value of each spaxel. The axis ratios calculated using GALFIT are sensitive to the choice of point-spread function (PSF), however there is little (if any) precedent for using GALFIT with IFS data. We require a PSF which has been observed in a similar manner as our galaxies. To achieve this we observed an A-type star

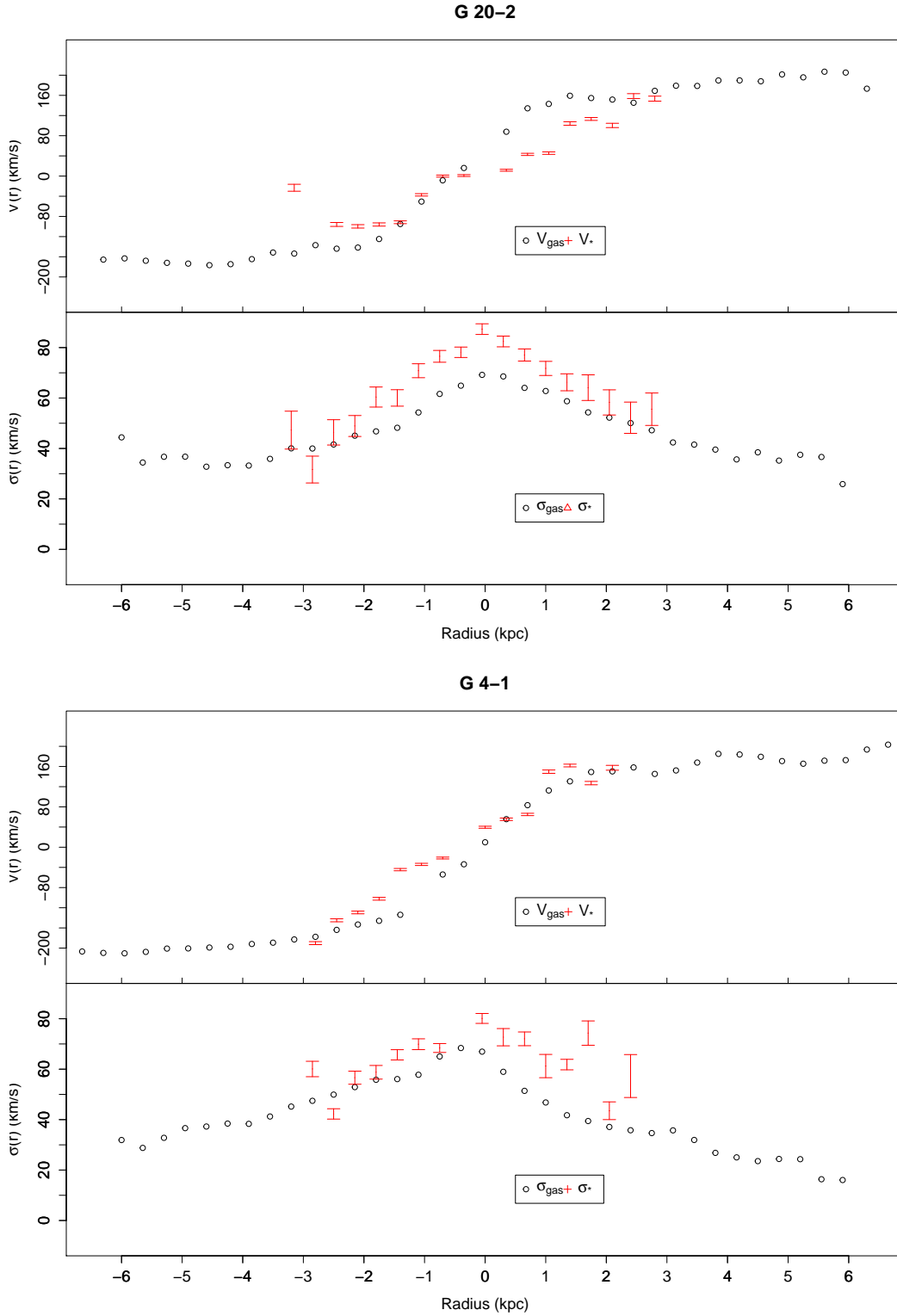


**Figure 10.** Galaxy rotation curves and  $\sigma$  profiles averaged in bins of 300 pc. Velocities are plotted with a correction for angular dependence using  $V(r, \phi) = V(r) \cos(\phi) \sin(i)$  where  $\phi$  is the angle between a given spatial location and the semimajor axis with the center of the galaxy as the vertex and  $i$  is the galaxy inclination. For  $\sigma$  we have subtracted our beam smearing estimate from the observed velocity dispersion in quadrature on a bin by bin basis. We overplot values for the emission line kinematics (black circles) and stellar kinematics (red error bars) extracted during our pPXF procedure. For the emission line measurement, we probe well into the flat portion of the rotation curve where the effects of beam smearing are negligible while stellar kinematics measurements just reach this region. The size of the error bars plotted for our stellar kinematics indicate the average of our simulated uncertainties in each bin.

with GMOS in IFS mode with the spectral range chosen to match the rest frame wavelengths of our galaxy observations. This data was reduced in the same manner as described in Section 2.3. We created a median image of this star from the reduced data cube and used this as our PSF while fitting with GALFIT. We consider this the best possible method for defining the IFS response to a point source. We report the axis ratios (b/a) we recover, as well as inclinations calculated using the standard equation in Table 1.

Figure 10 shows the computed rotation curves and velocity dispersion profiles for our galaxies. Both the ionized-gas (open circles) and stellar (red error bars) kinematics are measured out to the flat portion of the rotation curves of these galaxies. This allows us to make robust estimates of global velocity dispersions. In all bins, the velocity curves of both components are well matched with small differences likely due to differences in binning between our gas and stellar kinematics fitting procedures. Large differences seen in the rotation curves of G 20-2 are possible indications of asymmetric drift. Stellar velocity dispersions in most bins agree with the ionized gas velocity dispersions within our simulated uncertainties (indicated by the size of the error bars) or are found to be slightly higher. This suggests that the observed turbulence in the ionized gas in DYNAMO galaxies is not primarily due to star-formation feedback. If the turbulence was due to feedback, stellar velocity dispersion measurements would be *lower* than that of the gas.

### 3.6 Results Summary

The optical spectra of these galaxies are dominated by young stellar populations. Figure 4 shows that the absorption spectrum is dominated by Balmer lines. These lines are strongest in B and A type stars which dominate optical spectra of SSP's at ages younger than 1 Gyr. This is consistent with the young ages (500 Myr) of templates selected for our stellar kinematics fitting. These young ages, along with the dynamically hot kinematics, high rates of star formation (Green et al. 2014), and large gas fractions (Fisher et al. submitted) are suggestive of early stages of disk-galaxy evolution. Such an evolutionary state is more characteristic of star-forming galaxies at high redshift than star-forming galaxies at  $z < 1$ .

We map the relative strength of emission line and continuum flux which reveals clumpy substructure which was not resolved in previous observations (Figure 1). Both galaxies exhibit multiple regions of high emission-line equivalent width located 1-2 kpc from a single, centrally located peak in continuum emission. The discovery of these clumps lends further support to the suggestion that these galaxies are low redshift analogues to clumpy galaxies at  $z \sim 2$ .

We find that the kinematics of the stellar and ionized gas components of these galaxies are well matched, with large stellar velocity dispersions similar to ionized gas velocity dispersions found in previous work (Green et al. 2014). This is indicative of a scenario in which the ionized gas turbulence is driven externally rather than being primarily due to star-formation feedback. This result is also found in a recent IFS study of galactic winds in local luminous and ultraluminous infrared galaxies (LIRGS/ULIRGS) (Arribas et al. 2014). Measuring winds from H $\beta$  using our GMOS datacubes is inherently difficult due to the complex absorp-

tion profile also associated with this transition. Emission line profiles of [OIII] (5007 Å) in galaxy G 20-2 show some evidence for broad components which could be indicative of star-formation driven winds expected in such high-SFR systems (see Section 4.4 for some discussion). Inclusion of a broad component however, has a negligible effect on velocity dispersion measurements of the narrow component when compared to a single component fit. Therefore not including a broad component in fits presented here will not affect our conclusions. An analysis of the broad components of emission lines of DYNAMO galaxies will be presented in future work based on IFS observations of Paschen  $\alpha$  using Keck OSIRIS.

## 4 DISCUSSION

### 4.1 Comparison With Local Disks

In Figure 11, we show that our ionized-gas velocity-dispersion measurements are truly unusual compared to similar measurements of low-redshift late-type galaxies. We established this difference based on comparison with the IFS studies from the DiskMass survey of Andersen et al. (2006), who examine the H $\alpha$  linewidths of 39 nearby, face-on disks using the DensePak instrument on the WIYN 3.5 m telescope. We obtained H $\alpha$ -line-width measurements from each fiber from their observations to compare directly with our H $\beta$  measurements in each of our spatial bins from Figure 6. We plot in Figure 11 the cumulative fractions of velocity dispersion for the two samples.

It is clear from Figure 11 that the disk galaxies considered here are outliers relative to local disk samples. The disk velocity dispersions of  $\sim 32$  km s $^{-1}$  we measure for our sample are in the 98<sup>th</sup> percentile of individual fiber measurements for the sample of Andersen et al. (2006). We note, however, that galaxies in Andersen et al. (2006) were selected in part for their face-on inclinations, an orientation which will produce the lowest possible measurements of velocity dispersion due to a minimal contribution from velocity dispersions within the plane of the disk. While this may bias their results to low  $\sigma$  measurements, theirs represents the best comparison sample currently available.

We also compare with the recent IFS studies of Bellocchi et al. (2013) and Arribas et al. (2014) who observe ionized gas kinematics of LIRGS/ULIRGS at redshifts comparable to those of the DYNAMO sample. Galaxies such as these represent the most extremely star-forming local galaxies, and many galaxies in their sample have SFRs comparable to those of G 4-1 and G 20-2. Similar to the results presented here, Bellocchi et al. (2013) and Arribas et al. (2014) find enhanced ionized gas velocity dispersions relative to average local disk galaxies. At SFRs in the range observed for G 4-1 and G 20-2 ( $\sim 20$ - $40$  M $_{\odot}$  yr $^{-1}$ ), local LIRGS/ULIRGS typically have ionized gas velocity dispersions of  $\sim 60$ - $80$  km s $^{-1}$ , roughly 30 km s $^{-1}$  higher than ionized gas velocity dispersions we measure for G 4-1 and G 20-2. This is likely due to the fact that the LIRG/ULIRG sample studied by Bellocchi et al. (2013) and Arribas et al. (2014) include, in addition to disks, a significant fraction of interacting systems and mergers. Considering only a sub-sample of non-interacting, non-AGN disk LIRGs, Arribas et al. (2014) find

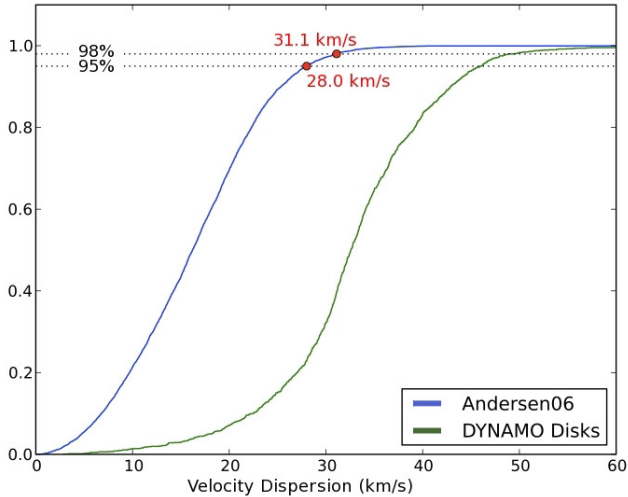


**Figure 11.** Cumulative fraction in  $\sigma$  for each fiber from Andersen et al. (2006) compared with each value from outer spatial bins indicated in Figure 6 for both galaxies considered here. It is clear that values measured for G 20-2 and G 4-1 do not come from the same parent sample as those measured for local face on spirals. Indeed, the values of  $\sigma_{d, gas}$  measured for these galaxies are in the 98<sup>th</sup> percentile of individual fibers from Andersen et al. (2006).

$\sigma \simeq 45 \text{ km s}^{-1}$ , comparable to the findings presented here for DYNAMO disks.

## 4.2 Stellar Kinematics and Disk Thickness

Both the ionized-gas and young-stellar components are observed to have similarly high velocity dispersions (compared to a velocity dispersion of  $\sim 10 \text{ km s}^{-1}$  observed for young stars in the Milky Way, Wielen 1977; Seabroke & Gilmore 2007). We suggest that the gas was already turbulent during the epoch in which the young, bright stars (which dominate the observed continuum emission) were formed. This is in contrast to a scenario in which the stars were formed from a gas cloud with a low velocity dispersion, which is subsequently inflated through stellar feedback to the turbulent-gas disks currently observed. To account for this initial turbulence, external sources of gas may be required. One possibility is that these galaxies are undergoing large amounts of gas accretion, which can drive turbulence through momentum or can induce turbulence through instabilities associated with gas rich disks (Dekel et al. 2009; Forbes et al. 2013; Bournaud et al. 2014).

What is the fate of the young stellar populations we observe in G 20-2 and G 4-1? It is difficult to significantly alter the stellar orbits in a galaxy short of a major merger. A violent event such as this, however, would *increase* the stellar velocity dispersions of the host galaxies involved (Dasyra et al. 2006; Schauer et al. 2014). We observe young stellar populations in G 20-2 and G 4-1 with large velocity dispersions suggesting a thick disk of stars. As this population ages, it will likely become a similarly thick distribution of old stars akin to thick disks observed in low-redshift disk galaxies. We suggest that these galaxies contain a young, thick disk, which is in the process of forming.

We have shown in Figure 3 that these galaxies are well

approximated by an exponential disk, allowing us to estimate their disk thicknesses by considering the vertical component of the stellar velocity dispersion. We calculate disk scale heights using the equation (van der Kruit & Freeman 2011):

$$h_z = \frac{\sigma_z^2}{c\pi G \Sigma_{\mathcal{M}_*}} \quad (2)$$

where  $h_z$  represents the scale height,  $\sigma_z$  is the vertical stellar velocity dispersion,  $G$  is the gravitational constant,  $\Sigma_{\mathcal{M}_*}$  is the stellar mass surface density, and  $c$  is an empirical constant which varies between  $3/2$  for an exponential disk and  $2$  for an isothermal distribution. Here we choose a value of  $3/2$  which is often used in studies of disk galaxies. We calculate our stellar mass surface density using:

$$\Sigma_{\mathcal{M}_*}(r) = \frac{\mathcal{M}_*}{2\pi h^2} e^{-r/h} \quad (3)$$

Where  $\mathcal{M}_*$  is the total stellar mass,  $r$  is the radius, and  $h$  is the exponential disk scale length. We take previously reported stellar masses from Table 1, and we determine scale lengths from exponential disk fits presented in Figure 3 and also reported in Table 1. Evaluating Equation 3 at the average radius of our  $\sigma_{d,*}$  measurements results in  $\Sigma_{\mathcal{M}_*}$  values of 198 and  $650 \text{ M}_\odot \text{ pc}^{-2}$  for G 20-2 and G 4-1 respectively.

What remains is to determine values of  $\sigma_z$  from our observed velocity dispersions. The disk velocity dispersions reported in Section 3.3.3 are line of sight values which contain a contribution from the radial and tangential velocity dispersions ( $\sigma_R$  and  $\sigma_\phi$ ). We can recover the vertical component of velocity dispersion using the equation (Shapiro, Gerssen & van der Marel 2003):

$$\sigma_{\text{los}}^2 = [\sigma_R^2 \sin^2 \theta + \sigma_\phi^2 \cos^2 \theta] \sin^2 i + \sigma_z^2 \cos^2 i \quad (4)$$

with  $i$  representing the inclination angle (determined from axis ratios measured with GALFIT, Peng et al. 2002) and  $\theta$  the position angle from the major axis in the plane of the disk. To isolate  $\sigma_z$  we consider the ratios  $\alpha \equiv \sigma_z/\sigma_R$  and  $\beta \equiv \sigma_\phi/\sigma_R$ . Combining these with Equation 4 and taking an average over  $\theta$  results in:

$$\sigma_z = \frac{\sigma_{\text{los}}}{\cos i} \left( 1 + \frac{(\beta^2 + 1) \tan^2 i}{2\alpha^2} \right)^{-1/2} \quad (5)$$

From kinematics observations of the Solar Neighborhood these values are found to be  $0.5 < \alpha < 0.6$  and  $0.6 < \beta < 0.7$  for the thin disk of the Milky Way. While it is likely that observations of radially decreasing vertical velocity dispersions will be reflected in  $\alpha$  and  $\beta$ , radial dependence of these values has yet to be measured (Bershady et al. 2010).

Measurements of  $\alpha$  and  $\beta$  in external galaxies are also limited. The best example is that of Shapiro, Gerssen & van der Marel (2003), who compare integrated velocity dispersions along the major and minor axes of 6 nearby spiral galaxies from spectroscopic observations allowing them to measure  $\alpha$  directly. This results in  $0.5 < \alpha < 0.8$  increasing with Hubble type from Sc to Sa. This increase, however, could simply be a result of an increased influence of the bulge at earlier types. Values for later types are found in

**Table 4.** Stellar Disk Thicknesses

Galaxy	$\sigma_{\text{los}}$ km s <sup>-1</sup>	$\sigma_z$ km s <sup>-1</sup>	$h_{z,\text{los}}$ pc	$h_{z,\text{corr}}$ pc
G 4-1	47.5	41.6	171	131
G 20-2	53.0	47.5	700	562

the range  $0.5 < \alpha < 0.7$  in agreement with measurements of van der Kruit & de Grijs (1999), who measure  $\alpha$  of 36 edge-on, late type galaxies (Sb - Sd) from photometry using empirical relations of Bottema (1993).

As discussed previously, our large values of  $\sigma_{c,*}$  may be influenced by a young galactic bulge. Thus for estimating the thickness of our galactic disks we take  $\sigma_{\text{los}} = \sigma_{d,*}$ . For our inclination corrections we take  $\alpha = 0.6$  and  $\beta = 0.7$ , but we note that these values are based on assumptions that may be invalid for young, marginally stable disks.

We believe it is reasonable to assume that velocity dispersions during disk assembly are closer to isotropic, forcing  $\alpha$  and  $\beta$  to values closer to 1. In the limit  $\alpha = \beta = 1$ , Equation 5 reduces to  $\sigma_z = \sigma_{\text{los}}$ . The large scale rotation in these galaxies suggests that the true value of  $\sigma_z$  will fall somewhere between our inclination corrected value and  $\sigma_{\text{los}}$ . We present our disk height calculations in Table 4 using both  $\sigma_z$  and  $\sigma_{\text{los}}$  in Equation 2.

We compare estimates of disk scale heights presented here with Yoachim & Dalcanton (2006) who fit two component (thin plus thick) disk models to R-band photometry of local edge-on, late-type galaxies. The disk heights we estimate for G 20-2 (562-700 pc) are consistent with the high end of thin disk scale heights and the low end for thick disks. Our scale height estimate for G 4-1, however, is well within the thin disk regime. A caveat to our scale height estimates is that they are very dependent on our assumptions which are based on normal disk galaxies. These assumptions may not be valid for turbulent, gas-rich disks such as those studied here. We also note that estimates of the thin disk scale height of the Milky Way range 200-300 pc (van der Kruit & Freeman 2011).

An age dependence of stellar disk scale height is predicted by the simulations Bird et al. (2013) who find that the kinematics of a stellar population are inherited at birth. Stars formed early are scattered by gas rich mergers (or by interactions with clumps Elmegreen & Struck 2013) to kinematically hot orbits. The combination of young SSP ages and large velocity dispersions we measure from GMOS-IFS data for galaxy G 20-2 are consistent with the early stages of disk formation in the simulations of (Bird et al. 2013).

### 4.3 Stellar Populations

The star light that we measure in our sample is dominated by A type stars which are responsible for the strong Balmer absorption we observe (See Figure 4). From evolutionary studies of single stellar population models it is known that the spectra of galaxies change most significantly at early times as short lived massive stars evolve off the main sequence. In particular we have inferred from visual inspection of the PÉGASE templates that the A-star-dominated phase occurs approximately between 1 Myr and 1 Gyr. This qual-

itative assessment is consistent with the ages of our sample from spectral fitting using a full set of PÉGASE templates with ages ranging from 1 Myr to 20 Gyr (see Section 3.2). From this procedure we infer a SSP age of 500 Myr to be consistent with the stellar population which dominates the continuum flux in our galaxies.

It is most likely that our galaxies also host an older, less luminous, underlying stellar population. Apart from strong Balmer absorption lines, we also observe absorption associated with iron which must be produced in supernovae indicating multiple generations of stars. Regardless, by fitting our spectra using spectral templates of young SSPs we are measuring the kinematics of the young stars which are more closely associated with the strongly emitting ionized gas.

Figure 4 demonstrates that there is no obvious difference between the underlying shape of the continuum spectra between the regions of strongest H $\beta$  emission and the central regions. The only major difference is the equivalent width of H $\beta$  emission which is likely due to a local difference in specific star formation rate. This suggests that the stellar populations contributing the largest portion of the observed flux in our sample are similar across the extent of our galaxies, with ages around 500 Myr.

### 4.4 Fate of Star-Forming Clumps

We observe previously unresolved clumps of ionized gas within our galaxies (see Figure 1) which are completely absent from the stellar light mapped by continuum emission. The fate of these star-forming clumps is still uncertain. Due to their high star formation rates it has been suggested that clumps such as these will be dissolved by stellar feedback before they are able to migrate into the centers of their host galaxies (Murray, Quataert & Thompson 2010; Genel et al. 2012). Previous studies of outflows in high redshift clumpy galaxies have estimated clump lifetimes in the range between 10 and 200 Myr (Elmegreen et al. 2009; Genzel et al. 2011; Newman et al. 2012; Wuyts et al. 2012). This is younger than the  $\chi^2/\text{DOF}$  selected SSP age of our galaxies of 500 Myr. Figure 5 shows however that SSP ages as young as 60 Myr also provide reasonable kinematics fits.

We briefly mentioned in Section 3.6 that we observe evidence of a broad component in the [OIII] (5007 Å) emission line in galaxy G 20-2, possibly indicative of galactic scale winds. To investigate this we create a flux-weighted mean spectrum of G 20-2 while removing emission line broadening associated with large scale rotation by shifting each spaxel spectrally based on the ionized gas velocity map presented in Figure 6. We then fit [OIII] (5007 Å) with a double Gaussian profile composed of a narrow and a broad component, the latter being commonly associated with gas outflows (e.g. Westmoquette et al. 2012; Arribas et al. 2014). We measure a broad component with a velocity dispersion of 84 km s<sup>-1</sup> which is redshifted relative to the narrow component by 5.5 km s<sup>-1</sup>. Comparing with similar measurement of LIRGs/ULIRGs from Arribas et al. (2014) we conclude that this is evidence for weak galactic winds. This is consistent with a scenario in which the galactic scale turbulence is not primarily driven by star formation feedback, a result we previously inferred based on stellar versus gas kinematics.

Reliably fitting a two component emission line profile to the Balmer emission lines in our galaxies is hampered by the

complex shape of the corresponding strong absorption lines. For this reason, we defer further analysis of galactic scale winds to future work which will be based on Keck OSIRIS observations of Paschen  $\alpha$ . We note here however, that the velocity dispersion of the narrow component of [OIII] (5007 Å) in the integrated spectra of G 20-2 is  $40.0 \text{ km s}^{-1}$ , consistent with mean values presented in Section 3.4. This suggests that our results are not significantly affected by the absence of a broad component in our emission line fitting procedure.

The smooth appearance of the continuum images of our galaxies would appear to favor of short clump lifetimes, however this is not necessarily the case. In the simulations of Bournaud et al. (2014), large gas outflow rates from massive ( $>10^8 M_{\odot}$ ) clumps are matched by large amounts of gas accretion. This allows clumps to survive long enough to spiral into the center of their host galaxy while retaining a constant mass. These simulations predict that this process should be complete for most clumps (excluding those formed at large radii) in less than 500 Myr. During infall the old stellar component of these clumps will continually be stripped, possibly fueling thick disk formation. Therefore, if these simulations are representative of the galaxies presented here, the smooth appearance of the continuum images is not a strong argument against long lived clumps. Such a scenario is consistent with the theoretical work of Dekel et al. (2013).

We show in Section 3.3.2 that the large velocity dispersions we measure in the central regions of G 20-2 and G 4-1 are not caused by beam smearing. We suggest that this is possible evidence for a young bulge or pseudobulge formed from inspiralling clumps. From long slit spectroscopy of the bulges of local late type galaxies, Fabricius et al. (2012) find velocity dispersions ranging from 50-200  $\text{km s}^{-1}$  consistent with central stellar velocity dispersions presented here ( $\sigma_{c,*} = 66.3$  and  $58.0 \text{ km s}^{-1}$ ). In particular, they find that pseudobulges (as indicated by low Sérsic indices and nuclear morphology that is similar to disks) have central stellar velocity dispersion of 50-150  $\text{km s}^{-1}$  with an average of  $\sim 100 \text{ km s}^{-1}$ . We note that the largest stellar velocity dispersions we measure for single spaxels in the centers of G 20-2 and G 4-1 are  $\sim 80 \text{ km s}^{-1}$  after correcting for beam smearing.

In both of our galaxies the bulge-disk decomposition of the stellar surface brightness profiles result in bulges with very low Sérsic index ( $n_b \sim 0.5 - 0.8$ ); typically low Sérsic indices are indicative of pseudobulges in nearby galaxies (Fisher & Drory 2008). However the bulges in our galaxies have significant differences compared to those typical of low redshift samples. Both galaxies, particularly G20-2, are more compact than typical of pseudobulges (Fisher & Drory 2010). Also it is difficult to interpret the properties of our bulges as the central starburst in each galaxy may affect the mass-to-light ratios. Nonetheless, a plausible scenario may be that pseudobulges (or at least pseudobulges in S0-Sb galaxies) are constructed through multiple mechanisms including early build up from clumps and in more recent epochs from secular evolution. This may be supported both by the near ubiquity of clumpy galaxies at high redshift (Tacconi et al. 2013) and pseudobulge galaxies at low redshift (Fisher & Drory 2011). In this case, we may be observing the early stages of pseudobulge formation in our target galaxies.

Considering both morphological and dynamical infor-

mation obtained from GMOS-IFS data we find that galaxies G 20-2 and G 4-1 are consistent with an early evolutionary state of massive late-type galaxies characterized by rapid bulge growth through the infall of gas rich clumps.

#### 4.5 Analogues to High Redshift Clumps?

We observe many similarities between our galaxies and clumpy galaxies observed at high redshift. Galaxies in the DYNAMO sample were initially selected for their extreme  $H\alpha$  emission (and thus extreme star formation) while excluding AGN (Green et al. 2014). Resolved kinematic measurements reveal a number of them to exhibit smooth rotation and large velocity dispersions typical of high redshift samples (Genzel et al. 2008; Law et al. 2009; Swinbank et al. 2011; Wisnioski et al. 2012). Studies at both epochs have also inferred large sSFRs based on the Kennicutt-Schmidt relation (Kennicutt 1998). These findings imply large gas fractions which have subsequently been confirmed both at high redshift (Tacconi et al. 2010; Daddi et al. 2010; Tacconi et al. 2013) and in the DYNAMO sample (Fisher et al. submitted).

Furthermore, the GMOS observations presented here reveal two compact disk-like galaxies from DYNAMO host clumps similar to those observed at high redshift, providing further evidence of their similarity to high-redshift clumpy disks. False color images we produce highlighting the differences between emission line regions and the stellar continuum bear a striking resemblance to false color images of high redshift clumpy galaxies from Wuyts et al. (2012) which are of similar stellar mass to galaxies presented here. We note that this comparison may not be entirely fair, however, as their clumpy images are produced from rest frame ultraviolet rather than emission lines.

Quantitatively we find, based on preliminary measurements of DYNAMO HST imaging, that properties of individual DYNAMO clumps closely mirror those of clumps at high redshift. Both clump luminosity and size are the subject of a forthcoming paper to which we defer detailed analysis (Fisher et al. in prep). For DYNAMO galaxies G 04-1 and G 20-2 we find that individual clumps have luminosities ranging  $L_{H\alpha} \sim 10^{41} - 10^{43} \text{ erg s}^{-1}$  (corresponding to  $\sim 1 - 10 M_{\odot} \text{ yr}^{-1}$ ). These fluxes are significantly brighter than observations of local HII regions (Wisnioski et al. 2012; Livermore et al. 2012), and comparable to what is observed in clumps of high redshift galaxies (e.g. Genzel et al. 2008; Wisnioski et al. 2012).

## 5 SUMMARY

In this work we have presented the spatially-resolved stellar-kinematics measurements of two young, star-forming galaxies using IFS observations with the GMOS instrument at the Gemini Observatories. These galaxies are taken from the larger DYNAMO sample (Green et al. 2010, 2014) of extremely  $H\alpha$  luminous galaxies selected from SDSS DR4 as possible analogues of high-redshift clumpy disks.

Previous studies of these objects have shown them to contain a turbulent rotating disk of ionized gas. It was not known, however, if the source of this turbulence was feedback (e.g. driven by star-formation) or dynamical instabil-



ities (such as caused by a gas-rich disk). By showing that the kinematics of the ionised gas and the dominant, young stellar population are closely coupled we provide strong evidence for the latter scenario. Our findings can be summarized as follows:

- For galaxy G 20-2, we confirm that the previously reported gas turbulence is not an artifact of beam smearing or spatial resolution. For galaxy G 4-1 we find disk velocity dispersions  $\sim 20 \text{ km s}^{-1}$  lower than previously reported values. While beam smearing make a small contribution the difference is driven more by the low sensitivity of previous observations in the outer disk.
- In both galaxies, the rotation of the stars and ionized gas are closely coupled, and characterized by smooth rotation and large velocity dispersions. Velocity dispersions of both components are found to be  $\sim 10 \text{ km s}^{-1}$  larger than values measured in nearby disk galaxies ( $\sim 20 \text{ km s}^{-1}$ ).
- We have determined that the stellar populations which dominate the optical continuum light are composed of young stars with ages of 60-500 Myr. Their large stellar velocity dispersion ( $\sim 50 \text{ km s}^{-1}$ ) is in marked contrast to that of the young stellar population in the disk of the Milky Way ( $\sim 5\text{--}10 \text{ km s}^{-1}$  for  $< 1 \text{ Gyr}$ , Wielen 1977; Seabroke & Gilmore 2007).
- We resolve clumpy substructure in the ionized gas component of these galaxies that was not previously apparent. This supports the idea that these galaxies are analogous to young and clumpy disk galaxies at high redshift.

If the star formation in these galaxies is rapidly truncated and they continue to evolve in the absence of major mergers, they may eventually resemble S0 galaxies or the bulges of late type galaxies we see nearby. This is a likely outcome as it is difficult to significantly alter the velocity profile of the stellar component of a galaxy; the velocity dispersions of stellar populations are effectively inherited from the gas in which they formed. As star formation continues to gradually deplete the gas content, the gas disk will thin and produce future generations of stars with smaller scale heights. This scenario could also result in galaxies similar to the Milky Way, assuming that the stellar component we currently observe will become a thick disk of old stars. If the DYNAMO sample shares the same fate as high-redshift galaxies (as they share many physical properties) then it is possible that high-redshift clumpy disks truly represent progenitors of disks and S0 galaxies locally, as predicted by theory.

Support for this project is provided in part by the Victorian Department of State Development, Business and Innovation through the Victorian International Research Scholarship (VIRS). We also acknowledge support from ARC Discovery Project DP130101460. This work is based on observations obtained at the Gemini Observatory (programs GN-2011B-Q-54 and GS-2011B-Q-88), which is operated by the Association of Universities for Research in Astronomy, Inc., under a cooperative agreement with the NSF on behalf of the Gemini partnership: the National Science Foundation (United States), the National Research Council (Canada), CONICYT (Chile), the Australian Research Council (Aus-

tralia), Ministério da Ciência, Tecnologia e Inovação (Brazil) and Ministerio de Ciencia, Tecnología e Innovación Productiva (Argentina).

## REFERENCES

- Allington-Smith J., Murray G., Content R., Dodsworth G., Miller B. W., Turner J., Jorgensen I., Hook I., 2002, *Experimental Astronomy*, 13, 1
- Andersen D. R., Bershadsky M. A., Sparke L. S., Gallagher, III J. S., Wilcots E. M., van Driel W., Monnier-Ragaine D., 2006, *Astrophys. J., Suppl. Ser.*, 166, 505
- Arribas S., Colina L., Bellocchi E., Maiolino R., Villar-Martín M., 2014, *ArXiv e-prints:1404.1082*
- Baldwin J. A., Phillips M. M., Terlevich R., 1981, *Publ. Astron. Soc. Pac.*, 93, 5
- Bellocchi, E., Arribas, S., Colina, L., & Miralles-Caballero, D. 2013, *Astron. Astrophys.*, 557, A59
- Bershadsky M. A., Verheijen M. A. W., Westfall K. B., Andersen D. R., Swaters R. A., Martinsson T., 2010, *Astrophys. J.*, 716, 234
- Bird J. C., Kazantzidis S., Weinberg D. H., Guedes J., Callegari S., Mayer L., Madau P., 2013, *Astrophys. J.*, 773, 43
- Bottema R., 1993, *Astron. Astrophys.*, 275, 16
- Bournaud F., Elmegreen B. G., 2009, *Astrophys. J., Lett.*, 694, L158
- Bournaud F. et al., 2014, *Astrophys. J.*, 780, 57
- Cappellari M., Copin Y., 2003, *Mon. Not. R. Astron. Soc.*, 342, 345
- Cappellari M., Emsellem E., 2004, *Publ. Astron. Soc. Pac.*, 116, 138
- Ceverino D., Dekel A., Bournaud F., 2010, *Mon. Not. R. Astron. Soc.*, 404, 2151
- Chabrier G., 2003, *Publ. Astron. Soc. Pac.*, 115, 763
- Daddi E. et al., 2010, *Astrophys. J.*, 713, 686
- Dasyra K. M. et al., 2006, *Astrophys. J.*, 651, 835
- Davies R. et al., 2011, *Astrophys. J.*, 741, 69
- Dekel A. et al., 2009, *Nature*, 457, 451
- Dekel A., Zolotov A., Tweed D., Cacciato M., Ceverino D., Primack J. R., 2013, *Mon. Not. R. Astron. Soc.*, 435, 999
- Elmegreen B. G., 2011, in *EAS Publications Series*, Vol. 51, *EAS Publications Series*, Charbonnel C., Montmerle T., eds., pp. 59–71
- Elmegreen B. G., Elmegreen D. M., 2005, *Astrophys. J.*, 627, 632
- Elmegreen B. G., Elmegreen D. M., Fernandez M. X., Lemonias J. J., 2009, *Astrophys. J.*, 692, 12
- Elmegreen B. G., Struck C., 2013, *Astrophys. J., Lett.*, 775, L35
- Epinat B. et al., 2012, *Astron. Astrophys.*, 539, A92
- Fabricius M. H., Saglia R. P., Fisher D. B., Drory N., Bender R., Hopp U., 2012, *Astrophys. J.*, 754, 67
- Fisher D. B., Drory N., 2008, *Astron. J.*, 136, 773
- Fisher D. B., Drory N., 2010, *Astrophys. J.*, 716, 942
- Fisher D. B., Drory N., 2011, *Astrophys. J., Lett.*, 733, L47
- Forbes J. C., Krumholz M. R., Burkert A., Dekel A., 2013, *ArXiv e-prints:1311.1509*
- Förster-Schreiber N. M. et al., 2009, *Astrophys. J.*, 706, 1364
- Förster Schreiber N. M. et al., 2011, *Astrophys. J.*, 739, 45

- Genel S. et al., 2012, *Astrophys. J.*, 745, 11
- Genzel R. et al., 2008, *Astrophys. J.*, 687, 59
- Genzel R. et al., 2011, *Astrophys. J.*, 733, 101
- Glazebrook K., 2013, ArXiv e-prints:1305.2469
- Gnerucci A. et al., 2011, *Astron. Astrophys.*, 533, A124
- Golubov O. et al., 2013, *Astron. Astrophys.*, 557, A92
- Gonçalves T. S. et al., 2010, *Astrophys. J.*, 724, 1373
- Green A. W. et al., 2010, *Nature*, 467, 684
- Green A. W. et al., 2014, *Mon. Not. R. Astron. Soc.*, 437, 1070
- Guo Y., Giavalisco M., Ferguson H. C., Cassata P., Koekoemoer A. M., 2012, *Astrophys. J.*, 757, 120
- Hook I. M., Jørgensen I., Allington-Smith J. R., Davies R. L., Metcalfe N., Murowinski R. G., Crampton D., 2004, *Publ. Astron. Soc. Pac.*, 116, 425
- Hopkins A. M., Beacom J. F., 2006, *Astrophys. J.*, 651, 142
- Immeli A., Samland M., Gerhard O., Westera P., 2004, *Astron. Astrophys.*, 413, 547
- Kauffmann G. et al., 2003, *Mon. Not. R. Astron. Soc.*, 341, 54
- Kennicutt, Jr. R. C., 1998, *Astrophys. J.*, 498, 541
- Kereš D., Katz N., Weinberg D. H., Davé R., 2005, *Mon. Not. R. Astron. Soc.*, 363, 2
- Kroupa P., 2001, *Mon. Not. R. Astron. Soc.*, 322, 231
- Law D. R., Steidel C. C., Erb D. K., Larkin J. E., Pettini M., Shapley A. E., Wright S. A., 2009, *Astrophys. J.*, 697, 2057
- Le Borgne D., Rocca-Volmerange B., Prugniel P., Lançon A., Fioc M., Soubiran C., 2004, *Astron. Astrophys.*, 425, 881
- Lilly S. J., Le Fevre O., Hammer F., Crampton D., 1996, *Astrophys. J., Lett.*, 460, L1
- Liu G., Zakamska N. L., Greene J. E., Nesvadba N. P. H., Liu X., 2013, *Mon. Not. R. Astron. Soc.*, 430, 2327
- Livermore, R. C., Jones, T., Richard, J., et al. 2012, *Mon. Not. R. Astron. Soc.*, 427, 688
- Madau P., Ferguson H. C., Dickinson M. E., Giavalisco M., Steidel C. C., Fruchter A., 1996, *Mon. Not. R. Astron. Soc.*, 283, 1388
- Mandelker N., Dekel A., Ceverino D., Tweed D., Moody C. E., Primack J., 2013, ArXiv e-prints:1311.0013
- Martinsson T. P. K., Verheijen M. A. W., Westfall K. B., Bershadsky M. A., Schechtman-Rook A., Andersen D. R., Swaters R. A., 2013, ArXiv e-prints:1307.8130
- Murray N., Quataert E., Thompson T. A., 2010, *Astrophys. J.*, 709, 191
- Newman S. F. et al., 2012, *Astrophys. J.*, 761, 43
- Noguchi M., 1999, *Astrophys. J.*, 514, 77
- Pasetto S. et al., 2012, *Astron. Astrophys.*, 547, A70
- Peng C. Y., Ho L. C., Impey C. D., Rix H., 2002, *Astron. J.*, 124, 266
- Prugniel P., Soubiran C., 2001, *Astron. Astrophys.*, 369, 1048
- Schauer A. T. P., Remus R.-S., Burkert A., Johansson P. H., 2014, *Astrophys. J., Lett.*, 783, L32
- Schmidt M., 1959, *Astrophys. J.*, 129, 243
- Seabroke G. M., Gilmore G., 2007, *Mon. Not. R. Astron. Soc.*, 380, 1348
- Shapiro K. L., Gerssen J., van der Marel R. P., 2003, *Astron. J.*, 126, 2707
- Sobral D., Best P. N., Matsuda Y., Smail I., Geach J. E., Cirasuolo M., 2012, *Mon. Not. R. Astron. Soc.*, 420, 1926
- Swinbank A. M. et al., 2011, *Astrophys. J.*, 742, 11
- Tacconi L. J. et al., 2010, *Nature*, 463, 781
- Tacconi L. J. et al., 2013, *Astrophys. J.*, 768, 74
- Turner J. E. H., Miller B. W., Beck T. L., Song I., Cooke A. J., Seaman R. L., Valdés F. G., 2006, *New Astron. Rev.*, 49, 655
- van de Voort F., Schaye J., Booth C. M., Haas M. R., Dalla Vecchia C., 2011, *Mon. Not. R. Astron. Soc.*, 414, 2458
- van der Kruit P. C., de Grijs R., 1999, *Astron. Astrophys.*, 352, 129
- van der Kruit P. C., Freeman K. C., 2011, *Ann. Rev. Astron. Astrophys.*, 49, 301
- van Dokkum P. G., 2001, *Publ. Astron. Soc. Pac.*, 113, 1420
- Warner P. J., Wright M. C. H., Baldwin J. E., 1973, *Mon. Not. R. Astron. Soc.*, 163, 163
- Westmoquette M. S., Exter K. M., Smith L. J., Gallagher J. S., 2007, *Mon. Not. R. Astron. Soc.*, 381, 894
- Westmoquette, M. S., Clements, D. L., Bendo, G. J., & Khan, S. A. 2012, *Mon. Not. R. Astron. Soc.*, 424, 416
- Wielen R., 1977, *Astron. Astrophys.*, 60, 263
- Wisnioski E., Glazebrook K., Blake C., Poole G. B., Green A. W., Wyder T., Martin C., 2012, *Mon. Not. R. Astron. Soc.*, 422, 3339
- Wisnioski E. et al., 2011, *Mon. Not. R. Astron. Soc.*, 417, 2601
- Wright S. A., Larkin J. E., Law D. R., Steidel C. C., Shapley A. E., Erb D. K., 2009, *Astrophys. J.*, 699, 421
- Wuyts S. et al., 2012, *Astrophys. J.*, 753, 114
- Yoachim P., Dalcanton J. J., 2006, *Astron. J.*, 131, 226
- York D. G. et al., 2000, *Astron. J.*, 120, 1579